isvr Institute of Sound and Vibration Research

Sound Radiation from Plates with Mixed Impedance Boundary Conditions

A. Putra and D.J. Thompson

ISVR Technical Memorandum No 957

October 2005

University of Southampton

SCIENTIFIC PUBLICATIONS BY THE ISVR

Technical Reports are published to promote timely dissemination of research results by ISVR personnel. This medium permits more detailed presentation than is usually acceptable for scientific journals. Responsibility for both the content and any opinions expressed rests entirely with the author(s).

Technical Memoranda are produced to enable the early or preliminary release of information by ISVR personnel where such release is deemed to the appropriate. Information contained in these memoranda may be incomplete, or form part of a continuing programme; this should be borne in mind when using or quoting from these documents.

Contract Reports are produced to record the results of scientific work carried out for sponsors, under contract. The ISVR treats these reports as confidential to sponsors and does not make them available for general circulation. Individual sponsors may, however, authorize subsequent release of the material.

UNIVERSITY OF SOUTHAMPTON

INSTITUTE OF SOUND AND VIBRATION RESEARCH

DYNAMICS GROUP

Sound Radiation from Plates with Mixed Impedance Boundary Conditions

by

A. Putra and D.J. Thompson

ISVR Technical Memorandum No: 957

October 2005

Authorised for issue by
Professor M.J. Brennan
Group Chairman

Contents

1 Introduction **2**

2 Radiation efficiency of a baffled plate **6**

2.1 Spatial domain approach 6

2.1.1 Power radiated in terms of plate modes 6

2.1.2 Average over forcing points 9

2.2 Wavenumber domain approach 12

2.2.1 Governing equations 12

2.2.2 Singularity solution 17

2.3 The Fast Fourier Transform (FFT) based approach 19

2.3.1 Steps of calculation and bias error 19

2.3.2 Modified Green's function 20

2.4 Comparison of the baffled methods 23

2.4.1 Example results 23

2.4.2 Calculation time 28

3 Radiation efficiency of an unbaffled plate **29**

3.1 Iterative scheme using the FFT 29

3.1.1 Algorithm 29

3.1.2 Convergence problem 31

3.2 Wavenumber domain using modal basis 32

3.2.1 Derivation of equations 32

3.2.2 Integral solution using modal summation 35

3.3 Results and comparison with baffled plate 39

4 Radiation efficiency from a single point force position **43**

5 Conclusions **51**

References **53**

Chapter 1

Introduction

The sound radiation from vibrating structures plays an important role in the industrial world. Accurate prediction of sound radiation remains a challenging problem to solve for many situations. The sound radiation from structures is often determined in terms of plates, as many structures such as machinery casings, car compartments or body shells, hulls of ships, walls and floors of a building can be considered as plates.

A simplified model can be made by assuming a flat plate set in an infinite baffle, where the velocity of the plate is known, whereas the velocity is assumed to be zero on the baffle. The sound field above the plate can then be calculated by a Rayleigh integral approach [1]. The sound power can be found either by integrating the far field acoustic intensity over a hemisphere enclosing the plate or by integrating the acoustic intensity over the surface of the vibrating plate. A knowledge of the vibration velocity is required in both approaches. Since the modes of a plate with simply supported boundaries can readily be found analytically, such boundaries are often assumed to simplify the velocity field.

The radiation efficiency of a structure is defined as the ratio of the acoustic power radiated per unit area by a vibrating surface to that radiated by an infinite flat surface that is vibrating with the same average mean square velocity. The radiation efficiency is thus given by

$$\sigma = \frac{R_r}{\rho c S} = \frac{W}{\rho c S < \overline{v^2} >} \tag{1.1}$$

where R_r is the radiation resistance, W is the power radiated by the structure, ρ is the density of air, c is the speed of sound in air, S is area of the structure and $< \bar{v^2} >$ is its spatially averaged mean square normal velocity.

Many papers have been produced concerning the sound radiation of a baffled plate. Maidanik [2] worked on the radiation of a baffled plate for a broad-band case where the radiation resistance was determined as a frequency band average. Several approximate formulae were proposed for calculating the modal radiation resistance in the whole frequency range. Wallace [3] studied the radiation efficiency of a finite, simply supported rectangular plate in an infinite baffle determined theoretically from the total energy radiated to the farfield. The radiation efficiency was determined for individual modes. Asymptotic solutions for low frequencies were also presented. The results from Wallace were used by Xie *et al.* [4]. A summation over the contributions of individual modes was implemented to obtain the average radiation efficiency. It was found that using an average over force point locations, the cross-modal coupling terms average to zero.

Williams [5] used a scheme based on the Fast Fourier transform (FFT). Rayleigh's integral formula was evaluated numerically for baffled planar radiators, with specified velocity in the source plane using the FFT algorithm. The bias errors appearing using this technique were also described. Williams [6] also proposed a series expansion technique of the acoustic power radiated from planar sources. A MacLaurin expansion of the Fourier transform of the velocity was used to calculate the first few terms of the acoustic power.

The infinite rigid baffle frequently used as an approximation never exists in practical cases. A more practical situation for flat plates is an unbaffled plate. The problem of the radiation from an unbaffled flat plate is more difficult as the velocity is known over the plate surface whereas in the plane of the plate elsewhere the pressure is known (zero) and the velocity is unknown. However, several methods have been developed to solve the problem.

Atalla *et al.* [7] gave a numerical solution for the sound radiation of an unbaffled plate with general boundary conditions. The pressure jump was neglected when calculating the velocity of the plate allowing any boundary conditions to be derived analytically at the plate's edge. The simulation was compared with measurements and showed good agreement. However, the numerical implementation was found to be incorrect at high

frequencies due to convergence problems. Laulagnet [8] gave an alternative solution by presenting a double layer integral representation of the acoustic pressure. Both the pressure jump and the plate displacement were developed in terms of a series of the simply supported plate modes. The matrix of modal coupling coefficients was numerically calculated which later was used to define the accuracy of the radiation efficiency. In the paper, the author used the normalized cross-modal radiation impedance instead of the radiation efficiency. The real and imaginary parts of the radiation impedance were plotted for certain modes and were compared with those of the baffled plate. Measurements in air and water provided good validation of the theory.

Williams [9] applied an FFT based iterative technique to evaluate numerically the acoustic pressure and velocity on and near unbaffled thin plates vibrating in air. However, this technique suffers from convergence problems at low frequencies where the sound radiation of baffled and unbaffled plates shows significant differences. Oppenheimer and Dubowsky [10] introduced correction factors in the formula for a baffled plate and then used curve-fitting to determine various coefficients using measured results. Although practical, this method is not sufficiently rigorous to be considered in the present study.

More recently, Fahy and Thompson [11] have developed a wavenumber domain scheme involving inversion of a matrix equation. Intended for perforated plates, this method can also be applied to unbaffled plates. The acoustic pressure was defined as a function of the acoustic impedance which could be different above and beyond the plate region, creating the mixed impedance boundary conditions. The acoustic power was then calculated in the wavenumber domain.

Alternative approaches are available using numerical methods such as the finite element method (FEM) or boundary element method (BEM). These allow arbitrary geometry to be considered but do not provide the same physical insight as analytical methods. Several studies relating to the sound radiation have been proposed based on these methods. Nelisse *et al.* [12] proposed a study on the radiation of a baffled and an unbaffled plate with arbitrary boundary conditions dealing with a complete fluid-structure coupling. A Rayleigh-Ritz approach was used to develop the plate displacement in the baffled case, as well as the pressure jump in the unbaffled case. The radiation impedance was computed using a numerical approach based on the BEM. Nolte and Gaul [13] investigated the sound radiation from a vibrating structure in water. The pressure field in the fluid

domain and the velocity field were determined by using BEM with input data of surface velocities obtained from modal analysis from a FEM calculation. The sound radiation can be identified by either fluid-structure interaction or by intensity vector measurements in the acoustic near field. For a comparison, the sound radiation calculated by using BEM was compared with the results obtained by a superposition of pulsating spheres. Mattei [14] presented a formulation and a numerical solution using a simple BEM model of a boundary integral equation for a baffled plate, and also developed an analytical method for the constrained plate.

In this study the accuracy and computational efficiency of methods of Xie *et al.* [4], Fahy and Thompson [11], Williams [5], [9] and Laulagnet [8] for sound radiation from baffled and unbaffled plates are compared and their advantages and disadvantages are discussed. In a later phase, the modelling approach will then be extended to consider the sound radiation from a perforated plate, both in a baffle and unbaffled, in which the perforations are represented by an equivalent specific impedance, valid for holes that are small and relatively close together compared with the acoustic wavelength.

Chapter 2

Radiation efficiency of a baffled plate

Since plate vibrations generally involve many superimposed modes, the radiation efficiency of a plate, in principle, can be obtained by summing the effect of all the modes that contribute significantly in the frequency range under consideration [4]. Methods described in this chapter and also Chapter 3 apply this theory to obtain the averaged radiation efficiency of baffled and unbaffled plates. Simply supported plate boundaries will be considered for simplicity.

2.1 Spatial domain approach

2.1.1 Power radiated in terms of plate modes

Figure 2.1 shows a rectangular plate of length a and width b set in an infinite rigid baffle. Following the method of Xie *et al.* [4], by integrating the far field acoustic intensity over a hemisphere of radius r, for harmonic motion at frequency ω , the total acoustic power radiated can be written as

$$W = \int_0^{2\pi} \int_0^{\pi/2} \frac{|p(\mathbf{r})|^2}{2\rho c} r^2 \sin\theta \, d\theta \, d\phi \tag{2.1}$$

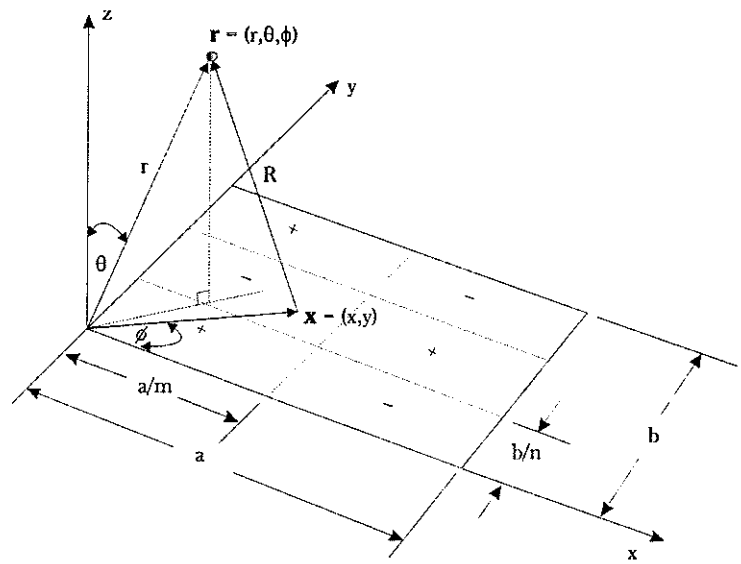

FIGURE 2.1: Co-ordinate system of a vibrating plate.

where $p(\mathbf{r})$ is the complex acoustic pressure amplitude at a location in space expressed in spherical co-ordinates, $\mathbf{r} = (r, \theta, \phi)$ at angular frequency ω, ρ is the density of air and c is the speed of sound.

The complex acoustic pressure amplitude $p(\mathbf{r})$ can be written in terms of the plate surface velocity using the Rayleigh integral [1] evaluated over the plate surface S, since the velocity is zero elsewhere on the baffle.

$$p(\mathbf{r}) = \frac{jk\rho c}{2\pi} \int_s v(\mathbf{x}) \frac{e^{-jkR}}{R} d\mathbf{x} \tag{2.2}$$

where $v(\mathbf{x})$ is the complex surface normal velocity amplitude at location $\mathbf{x} = (x, y)$, k is the acoustic wavenumber ($k = \omega/c$) and $R = |\mathbf{r} - \mathbf{x}|$ is the distance. A time dependence of $e^{j\omega t}$ is assumed.

The power radiated can also be calculated by integrating the acoustic intensity over the surface of the vibrating plate. The calculation is not developed further here as there are singularities when $R = 0$, hence more effort will be needed to overcome the problems in the Rayleigh integral. For further description of this approach, one can refer to the work proposed in reference [15] or [16].

The velocity $v(\mathbf{x})$ at any location $\mathbf{x}$ on the plate can be found by summing over all the modes of structural vibration of the plate.

$$v(\mathbf{x}) = \sum_{m=1}^{\infty}\sum_{n=1}^{\infty} u_{mn}\varphi_{mn}(\mathbf{x}) \tag{2.3}$$

where u_{mn} is the complex velocity amplitude of mode (m,n) which depends on the form of excitation and frequency. $\varphi_{mn}(\mathbf{x})$ is the value of the associated mode shape function at $\mathbf{x}$, and m,n are the indices of the modes.

For simply supported edges, the mode shape function $\varphi_{mn}(\mathbf{x})$ of the plate is defined by

$$\varphi_{mn}(x,y) = \sin\left(\frac{m\pi x}{a}\right)\sin\left(\frac{n\pi y}{b}\right) \tag{2.4}$$

By substituting Eq.(2.3) and (2.4) into Eq.(2.2), the sound pressure is thus given by

$$p(\mathbf{r}) = \sum_{m=1}^{\infty}\sum_{n=1}^{\infty} u_{mn}\left\{\frac{jk\rho c}{2\pi}\int_s \varphi_{mn}(\mathbf{x})\frac{e^{-jkR}}{R}d\mathbf{x}\right\} \tag{2.5}$$

or it can also be expressed as

$$p(\mathbf{r}) = \sum_{m=1}^{\infty}\sum_{n=1}^{\infty} u_{mn}A_{mn}(\mathbf{r}) \tag{2.6}$$

where $A_{mn}(\mathbf{r})$ is the term in the brackets in Eq.(2.5).

Wallace [3] has produced an analytical solution for $A_{mn}(\mathbf{r})$, which is given by

$$A_{mn}(\mathbf{r}) = jk\rho c\frac{e^{-jkr}}{2\pi r}\,\Phi \tag{2.7}$$

where

$$\Phi = \frac{ab}{\pi^2 mn}\left[\frac{(-1)^m e^{j\xi}-1}{(\xi/(m\pi))^2-1}\right]\left[\frac{(-1)^n e^{j\varrho}-1}{(\varrho/(n\pi))^2-1}\right]$$

$$\xi = ka\sin\theta\cos\phi, \quad \varrho = kb\sin\theta\sin\phi \quad \text{and} \quad r=|\mathbf{r}|$$

Since $u.u^* = \mid u \mid^2$, substituting Eq.(2.6) into Eq.(2.1) gives the total radiated power as

$$W = \sum_{m=1}^{\infty}\sum_{n=1}^{\infty}\sum_{m'=1}^{\infty}\sum_{n'=1}^{\infty}\left\{u_{mn}u^*_{m'n'}\int_0^{2\pi}\int_0^{\pi/2}\frac{A_{mn}(\mathbf{r})A^*_{mn}(\mathbf{r})}{2\rho c}r^2\sin\theta\,d\theta\,d\phi\right\} \tag{2.8}$$

where m' and n' denote m and n in the conjugate form. This equation shows that the total radiated power depends on the contributions of combination of modes. The contribution is usually referred to as the self-modal radiation for $m = m'$ and $n = n'$, and cross-modal radiation for either $m \neq m'$ or $n \neq n'$. According to Snyder and Tanaka [15], the cross-modal coupling can only occur (non-zero value) between a pair of modes with the same parity, i.e. both odd or both even in each x and y direction. Li and Gibeling [16] have investigated that the cross-modal coupling could have a significant impact on the radiated power, depending upon frequency and load condition. It is found that without taking its contribution into account, the sound power may be over- or under-estimated. However, Xie *et al.* [4] arrive at the conclusion that the contribution of the cross-modal coupling can be neglected when the plate is loaded with uncorrelated point forces averaged over all positions on the plate.

2.1.2 Average over forcing points

Following the procedure of [4], consider a point force applied on the plate at the location (x_0, y_0). To obtain the total radiated power, one can average the radiated power for all possible locations of uncorrelated point forces on the plate. This is written as

$$\overline{W} = \frac{1}{ab} \int_0^a \int_0^b W \, dx_0 \, dy_0 \tag{2.9}$$

Due to the orthogonality of the eigenfunctions, substituting Eq.(2.8) into Eq.(2.9) yields

$$\overline{W} = \sum_{m=1}^{\infty} \sum_{n=1}^{\infty} \left\{ \frac{1}{ab} \int_0^a \int_0^b u_{mn} u_{mn}^* \, dx_0 \, dy_0 \int_0^{2\pi} \int_0^{\pi/2} \frac{A_{mn}(\mathbf{r}) A_{mn}^*(\mathbf{r})}{2\rho c} r^2 \sin\theta \, d\theta \, d\phi \right\} \tag{2.10}$$

This verifies that the total radiated power is a summation of the power radiated by each single mode where the cross-modal coupling terms have now been eliminated. Eq.(2.10) can also be expressed as

$$\overline{W} = \sum_{m=1}^{\infty} \sum_{n=1}^{\infty} \overline{W}_{mn} \tag{2.11}$$

where $\overline{W}_{mn}$ is given by

$$\overline{W}_{mn} = \overline{|u_{mn}|^2} \int_0^{2\pi} \int_0^{\pi/2} \frac{A_{mn}(\mathbf{r}) A_{mn}^*(\mathbf{r})}{2\rho c} r^2 \, d\theta \, d\phi \tag{2.12}$$

and $\overline{|u_{mn}|^2}$ is the mean square of the modal velocity amplitude u_{mn}, averaged over all forcing positions.

From Cremer *et al.* [17], the modal velocity amplitude due to a point force applied at a location (x_0, y_0) is given by

$$u_{mn} = \frac{j\omega F \varphi_{mn}(x_0, y_0)}{[\omega_{mn}^2(1 + j\eta) - \omega^2]M_{mn}} \tag{2.13}$$

where F is the force amplitude, ω_{mn} is the natural frequency, η is the hysteretic damping factor, and M_{mn} is the modal mass which is

$$M_{mn} = \int_s \rho_s h \varphi_{mn}^2(x, y) dS = \frac{1}{4}\rho_s hab = \frac{M}{4} \tag{2.14}$$

where ρ_s, h and M are the density, thickness, and mass of the plate respectively.

Therefore $\overline{|u_{mn}|^2}$ can be calculated as

$$\overline{|u_{mn}|^2} = \frac{1}{ab}\int_0^a \int_0^b u_{mn} u_{mn}^* \, dx_0 \, dy_0 = \frac{4\omega^2 |F|^2}{[(\omega_{mn}^2 - \omega^2)^2 + \eta^2 \omega_{mn}^4]M^2} \tag{2.15}$$

The natural frequencies ω_{mn} are given by

$$\omega_{mn} = \left(\frac{B}{\rho_s h}\right)^{1/2} \left[\left(\frac{m\pi}{a}\right)^2 + \left(\frac{n\pi}{b}\right)^2\right] \tag{2.16}$$

where $B = Eh^3/[12(1 - \nu^2)]$ is the bending stiffness in the plate in which E is the Young's modulus and ν is the Poisson's ratio.

From Eq.(1.1) and Eq.(2.12), the modal radiation efficiency σ_{mn} is given by

$$\sigma_{mn} = \frac{\overline{W}_{mn}}{\rho c a b \overline{< |u_{mn}^2| >}} \tag{2.17}$$

where $\overline{< |u_{mn}^2| >}$ is the spatially averaged mean square velocity of a single mode averaged over all possible force positions given by

$$\overline{< |u_{mn}^2| >} = \frac{1}{S}\int_S \overline{|u_{mn}|^2} \, dx_0 \, dy_0 = \frac{\omega^2 |F|^2}{2[(\omega_{mn}^2 - \omega^2)^2 + \eta^2 \omega_{mn}^4]M^2} = \frac{\overline{|u_{mn}|^2}}{8} \tag{2.18}$$

Substituting Eq.(2.12) and (2.18) into (2.17) yields

$$\sigma_{mn} = 4 \int_0^{2\pi} \int_0^{\pi/2} \frac{A_{mn}(\mathbf{r}) A_{mn}^*(\mathbf{r})}{(\rho c)^2 ab} r^2 \, d\theta \, d\phi \tag{2.19}$$

After algebraic manipulation, Eq.(2.19) can be expressed as

$$\sigma_{mn} = \frac{64abk^2}{\pi^6 m^2 n^2} \int_0^{2\pi} \int_0^{\pi/2} \Theta \, \sin\theta \, d\theta \, d\phi \tag{2.20}$$

where

$$\Theta = \left\{ \frac{\begin{matrix} \cos(\xi/2) & \cos(\varrho/2) \\ \sin(\xi/2) & \sin(\varrho/2) \end{matrix}}{[(\xi/m\pi)^2 - 1][(\varrho/n\pi)^2 - 1]} \right\}^2$$

$\cos(\xi/2)$ and $\sin(\xi/2)$ are used when m is an odd or even integer respectively. Similarly, $\cos(\varrho/2)$ and $\sin(\varrho/2)$ are used when n is an odd or even integer respectively.

Since $\sin(\xi/2 + p\pi/2) = \pm \cos(\xi/2)$ and $\sin(\xi/2 + q\pi/2) = \pm \sin(\xi/2)$ where p is odd and q is even, Θ can be expressed more efficiently as

$$\Theta = \left\{ \frac{\sin(\xi/2 + m\pi/2) \sin(\xi/2 + n\pi/2)}{[(\xi/m\pi)^2 - 1][(\varrho/n\pi)^2 - 1]} \right\}^2 \tag{2.21}$$

As an example, Figure 2.2 plots the radiation efficiency of modes (1,1) and (10,1) of a rectangular plate having dimensions 0.65×0.5×0.003 m (details given in Section 2.4) in terms of normalised frequencies k/k_{mn}, where $k_{mn} = \sqrt{(m\pi/a)^2 + (n\pi/b)^2}$. The frequency resolution is 40 points per decade, spaced logarithmically. The doubled integral in Eq.(2.20) is evaluated using a built-in function in MATLAB implementing the two-dimensional Simpson quadrature with various error tolerances, e. The results show that the radiation efficiency increases as the frequency increases and then slowly converges to unity above the maximum peak. The better e used, the better the curve converges.

Finally, the general average radiation efficiency σ is then given by

$$\sigma = \frac{\sum_{m=1}^{\infty} \sum_{n=1}^{\infty} \overline{W}_{mn}}{\rho c a b \overline{< v^2 >}} = \frac{\sum_{m=1}^{\infty} \sum_{n=1}^{\infty} \sigma_{mn} \overline{< |u_{mn}^2| >}}{\overline{< v^2 >}} \tag{2.22}$$

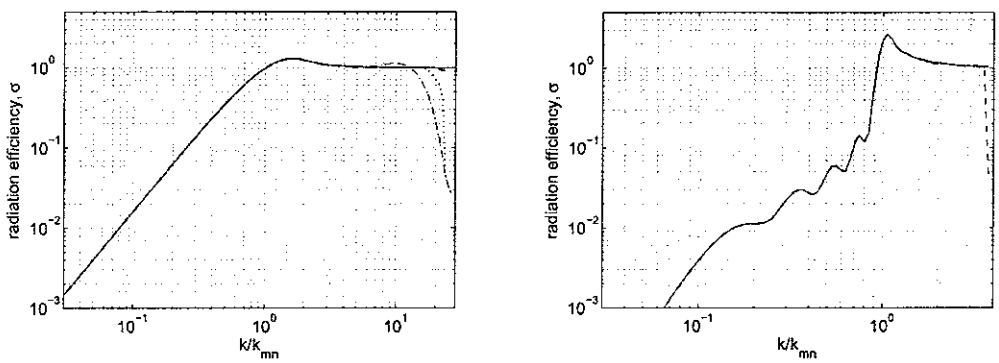

FIGURE 2.2: Radiation efficiency of (a) mode (1,1) and (b) mode (10,1) of a simply supported baffled plate using the spatial domain approach: e=10^{-3}(−−), 10^{-5}(···), 10^{-7}(−·−), 10^{-9}(—).

where $\overline{< \overline{v^2} >}$ is the result of summation of the spatially averaged modal mean square velocity $\overline{< \overline{|u_{mn}^2|} >}$, i.e. [17]

$$\overline{< \overline{v^2} >} = \sum_{m=1}^{\infty} \sum_{n=1}^{\infty} \overline{< \overline{|u_{mn}^2|} >} \tag{2.23}$$

Therefore

$$\begin{aligned} \sigma &= \frac{\sum_{m=1}^{\infty} \sum_{n=1}^{\infty} \sigma_{mn} \overline{< \overline{|u_{mn}^2|} >}}{\sum_{m=1}^{\infty} \sum_{n=1}^{\infty} \overline{< \overline{|u_{mn}^2|} >}} \\ &= \frac{\sum_{m=1}^{\infty} \sum_{n=1}^{\infty} \sigma_{mn} [(\omega_{mn}^2 - \omega^2)^2 + \eta^2 \omega_{mn}^4]^{-1}}{\sum_{m=1}^{\infty} \sum_{n=1}^{\infty} [(\omega_{mn}^2 - \omega^2)^2 + \eta^2 \omega_{mn}^4]^{-1}} \end{aligned} \tag{2.24}$$

Example results of σ will be given in Section 2.4 below.

2.2 Wavenumber domain approach

2.2.1 Governing equations

The sound radiation from a mode of vibration of a finite plate set in an infinite baffle can also be determined by wavenumber decomposition of the spatial distribution of velocity in the mode [18].

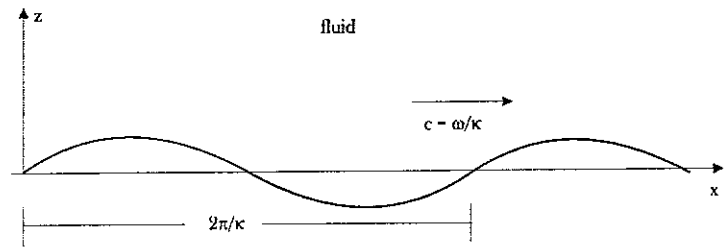

FIGURE 2.3: Propagating wave in a plate

Consider first a two-dimensional infinite vibrating plate, having velocity v, which is in contact with a fluid in the semi-infinite space $z > 0$ as shown in Figure 2.3. A plane transverse wave is travelling in the plate with arbitrary frequency ω and wavenumber κ. Sound is radiated by the plate into the fluid with the same wavenumber component in the x direction.

As the propagation of a plane wave in a two-dimensional space is expressed by

$$p(x, z, t) = p\, e^{-j(\kappa x + k_z z)} e^{j\omega t} \tag{2.25}$$

the condition must be satisfied that $\kappa < k$, i.e. the plate wave speed is greater than the speed of sound in the fluid, to allow the wave to propagate away from the plate surface. Also to fulfill this distinct condition, the positive sign must be chosen for k_z, whereas the negative sign is disallowed as no wave can propagate toward the surface of the plate.

The acoustic variable of the fluid in the x direction must be the same as that of the plate, i.e. $k_x = \kappa$ so that the wavenumber relationship is given by

$$k_z = \pm(k^2 - k_x^2)^{1/2} \tag{2.26}$$

where k is the acoustic wavenumber, $k = \omega/c$.

Consider the spatial Fourier transform of an arbitrary velocity distribution $v(x)$

$$\widetilde{V}(k_x) = \int_{-\infty}^{\infty} v(x) e^{-jk_x x} dx \tag{2.27}$$

and its inverse Fourier transform

$$v(x) = \frac{1}{2\pi}\int_{-\infty}^{\infty} \widetilde{V}(k_x)e^{jk_x x}dk_x \tag{2.28}$$

Thus if $v(x)$ represents the plate velocity, or zero on the baffle, the velocity distribution of a plate in a baffle can be expressed as an integral over wavenumber.

The radiated pressure field can be related to the surface normal velocity distribution through the specific acoustic impedance. The specific acoustic radiation impedance is defined as the ratio of complex amplitudes of pressure and particle velocity at a single frequency and wavenumber.

The linearized equation of momentum conservation in the z direction is given by

$$\rho\frac{\partial v_z}{\partial t} + \frac{\partial p}{\partial z} = 0 \tag{2.29}$$

where v_z is the component of particle velocity in the z direction and p is the pressure.

For harmonic motion at frequency ω, this gives in terms of complex amplitudes

$$j\omega\rho v_z(z) + \frac{dp}{dz} = 0 \tag{2.30}$$

Therefore for the case of the plane travelling wave given by Eq.(2.25), this yields

$$v_z = \frac{-1}{j\omega\rho}\frac{dp(z)}{dz} = \frac{k_z}{\omega\rho}p(z) \tag{2.31}$$

For a given wavenumber, the acoustic impedance can then be written as

$$z_a = \frac{p}{v_z} = \frac{\omega\rho}{k_z} \tag{2.32}$$

Thus in terms of the wavenumber transforms, Eq.(2.32) can be written as

$$z_a(k_x) = \frac{\widetilde{P}(k_x)}{\widetilde{V}(k_x)} = \frac{\omega\rho}{(k^2 - k_x^2)^{1/2}} \tag{2.33}$$

Considering now a plane wave travelling in the plate surface with a component in the x and y directions, having wavenumber components k_x and k_y, k_x^2 is then replaced by

$k_x^2 + k_y^2$. The direction of travel is at an angle $\theta = tan^{-1}(k_x/k_y)$ to the x-axis. Thus from Eq.(2.33), the surface pressure field wavenumber component related to the velocity wavenumber component is given by

$$[\widetilde{P}(k_x, k_y)]_{z=0} = \frac{\omega\rho}{(k^2 - k_x^2 - k_y^2)^{1/2}} \widetilde{V}(k_x, k_y) \tag{2.34}$$

Referring to Eq.(2.28) for a two-dimensional case, the surface pressure field and the surface normal velocity are

$$[p(x, y)]_{z=0} = \frac{1}{4\pi^2} \int_{-\infty}^{\infty} \int_{-\infty}^{\infty} [\widetilde{P}(k_x, k_y)]_{z=0} \, e^{j(k_x x + k_y y)} \, dk_x \, dk_y \tag{2.35}$$

$$v_n(x, y) = \frac{1}{4\pi^2} \int_{-\infty}^{\infty} \int_{-\infty}^{\infty} \widetilde{V}(k_x, k_y) \, e^{j(k_x x + k_y y)} \, dk_x \, dk_y \tag{2.36}$$

The power radiated is calculated by

$$\overline{W} = \frac{1}{2} \Re \left\{ \int_S p(x, y) \, v_n^*(x, y) \, dx \, dy \right\} \tag{2.37}$$

where $\Re$ denotes the real part.

Therefore by substituting Eq.(2.35) and (2.36) into (2.37) gives

$$\begin{aligned} \overline{W} = \frac{1}{32\pi^4} \Re \Bigg\{ \int_S \Bigg[\int_{-\infty}^{\infty} \int_{-\infty}^{\infty} [\widetilde{P}(k_x, k_y)]_{z=0} \, e^{j(k_x x + k_y y)} \, dk_x \, dk_y \\ \times \int_{-\infty}^{\infty} \int_{-\infty}^{\infty} \widetilde{V}^*(k_x', k_y') \, e^{-j(k_x' x + k_y' y)} \, dk_x' \, dk_y' \Bigg] \, dx dy \Bigg\} \end{aligned} \tag{2.38}$$

The range of double integration over the surface S can be changed from $-\infty$ to ∞ because the particle velocity v is ensured to be zero outside the plate boundary.

Thus substituting Eq.(2.34) into (2.38) gives

$$\begin{aligned} \overline{W} = \frac{1}{32\pi^4} \Re \Bigg\{ \int_{-\infty}^{\infty} \int_{-\infty}^{\infty} \Bigg[\int_{-\infty}^{\infty} \int_{-\infty}^{\infty} \frac{\omega\rho}{(k^2 - k_x^2 - k_y^2)^{1/2}} \widetilde{V}(k_x, k_y) \, e^{j(k_x x + k_y y)} \, dk_x \, dk_y \\ \times \int_{-\infty}^{\infty} \int_{-\infty}^{\infty} \widetilde{V}^*(k_x', k_y') \, e^{-j(k_x' x + k_y' y)} \, dk_x' \, dk_y' \Bigg] \, dx \, dy \Bigg\} \end{aligned} \tag{2.39}$$

If the integration is first performed over x and y, by changing the order of integration, the Dirac delta functions are obtained i.e.

$$\int_{-\infty}^{\infty}\int_{-\infty}^{\infty} e^{-j(k_x-k_x')x}e^{-j(k_y-k_y')y}dx\,dy = 4\pi^2\delta(k_x-k_x')\delta(k_y-k_y') \tag{2.40}$$

Hence Eq.(2.39) can be simplified as

$$\overline{W} = \frac{1}{8\pi^2}\Re\int_{-\infty}^{\infty}\int_{-\infty}^{\infty}\frac{\omega\rho}{(k^2-k_x^2-k_y^2)^{1/2}}\,|\widetilde{V}(k_x,k_y)|^2\,dk_x\,dk_y \tag{2.41}$$

In addition only wavenumber components satisfying the condition $(k_x^2+k_y^2)^{1/2} \leq k$ contribute to sound power radiation; elsewhere the term $(k^2-k_x^2-k_y^2)^{1/2}$ is imaginary. The range of integration can therefore be limited to give

$$\overline{W} = \frac{\rho c}{8\pi^2}\int_{-k}^{k}\int_{-\sqrt{k^2-k_y^2}}^{\sqrt{k^2-k_y^2}}\frac{k}{(k^2-k_x^2-k_y^2)^{1/2}}\,|\widetilde{V}(k_x,k_y)|^2\,dk_x\,dk_y \tag{2.42}$$

In the two-dimensional spatial Fourier transform, an individual mode velocity distribution is decomposed into a continuous spectrum of spatially harmonic, travelling plane wave components, each having a certain wavenumber vector which is given by

$$\widetilde{V}_{mn}(k_x,k_y) = \int_0^a\int_0^b u_{mn}\,\varphi_{mn}e^{-j(k_xx+k_yy)}\,dx\,dy \tag{2.43}$$

where $\widetilde{V}_{mn}(k_x,k_y)$ is the complex amplitude of the wavenumber component. Integration yields [18]

$$\widetilde{V}(\alpha,\beta) = u_{mn}\Lambda k^{-2}(\varepsilon+j\vartheta)(\gamma+j\varsigma) \tag{2.44}$$

where

$$\Lambda = \frac{\left(\frac{m\pi}{ka}\right)\left(\frac{n\pi}{kb}\right)}{\left[\alpha^2-\left(\frac{m\pi}{ka}\right)^2\right]\left[\beta^2-\left(\frac{n\pi}{kb}\right)^2\right]}$$

$$\varepsilon = (-1)^m\cos(\alpha ka)-1,\ \vartheta = (-1)^{m+1}\sin(\alpha ka)$$

$$\gamma = (-1)^n\cos(\beta kb)-1,\ \varsigma = (-1)^{n+1}\sin(\beta kb)$$

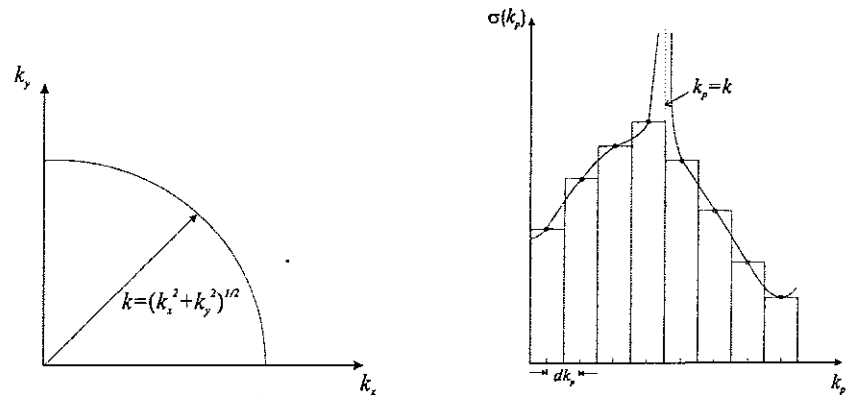

FIGURE 2.4: (a) Radiation circle and (b) Integration performed as a series of rectangles defining the area under the graph. The sample points are taken at the middle of the rectangles.

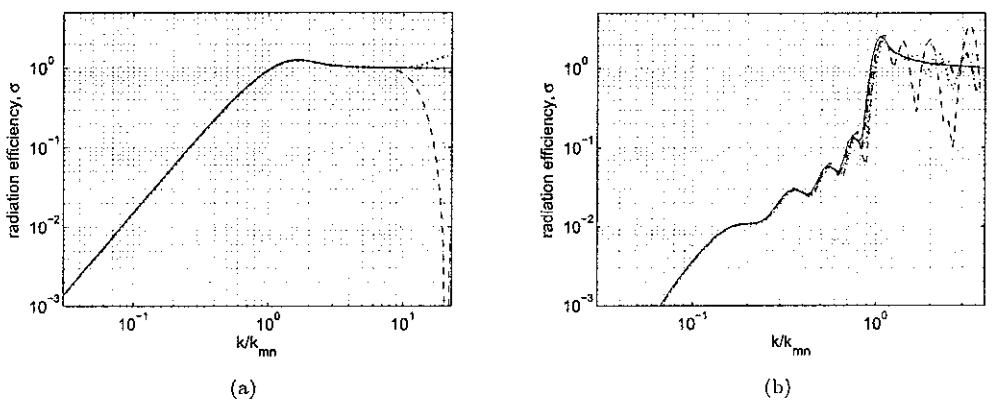

FIGURE 2.5: Radiation efficiency of (a) mode (1,1) and (b) mode (10,1) of a simply supported baffled plate using the wavenumber domain approach: $d\alpha = d\beta$ =0.20 (– –), 0.15 ($\cdots$), 0.09 (– · –), 0.05 (—) m.

efficiency converges as the sampling accuracy increases. It can also be seen that using the wavenumber domain approach, the results are exactly the same as the results of the spatial domain approach, given in Figure 2.2.

To find the average radiation efficiency over all modes, Eq.(2.24) can be applied. Example results are given in Section 2.4 below.

2.3 The Fast Fourier Transform (FFT) based approach

The Fourier transform of the velocity in the calculation, as defined in Eq.(2.27), can be solved much faster by using the Fast Fourier Transform (FFT). Compared with numerical integration of the conventional Fourier transform, the FFT can reduce the number of computations needed for N points from $2N^2$ to $2N \log_2 N$ [19]. In addition, as many programming languages, such as MATLAB, provide a built-in FFT function, the task of programming it is much reduced.

2.3.1 Steps of calculation and bias error

Williams [5] first implemented the numerical evaluation of the radiation efficiency using the FFT method. Rayleigh's integral formula can be evaluated for planar radiators of any shape, with any specified velocity in the source plane. Rayleigh's formula as expressed in Eq.(2.2) is rewritten by using a kernel[1]

$$h(x,y,d) = j\omega\rho g(x,y,d) = \frac{j\omega\rho}{2\pi}\frac{e^{-jk(x^2+y^2+d^2)^{1/2}}}{(x^2+y^2+d^2)^{1/2}} \tag{2.48}$$

where $g(x,y,d)$ is the half-space Green's function evaluated at $z = d$.

In convolution form, Rayleigh's formula can be expressed as

$$p(x,y,d) = v(x,y) \otimes h(x,y,d) \tag{2.49}$$

Thus by applying the convolution theorem, one can obtain

$$p(x,y,d) = \boldsymbol{F}^{-1}[\widetilde{V}(k_x,k_y)\widetilde{H}(k_x,k_y,d)] \tag{2.50}$$

where $\boldsymbol{F}^{-1}$ denotes the inverse Fourier transform, $\widetilde{V}$ is the Fourier transform of v and $\widetilde{H}$ is the Fourier transform of h, given by

$$\widetilde{H}(k_x,k_y,d) = j\omega\rho\widetilde{G}(k_x,k_y,d) = \omega\rho\frac{e^{-jk_z d}}{k_z} \tag{2.51}$$

[1]Note that Williams [5] uses the time dependence of $e^{-j\omega t}$ instead of $e^{j\omega t}$. This has been changed here for consistency with the remainder of this report

in which $\alpha = k_x/k$ and $\beta = k_y/k$ are the non-dimensional wavenumbers and a and b are the plate dimensions.

Referring to the co-ordinates in Figure 2.1 for wavenumber components, it is found that $k_x = k \sin\theta \cos\phi$ and $k_y = k \sin\theta \sin\phi$.

Thus by relating Eq.(2.44) to Eq.(2.7), it can also be found that

$$\widetilde{V}(k,\theta,\phi) = u_{mn} \frac{\Phi}{(ka)(kb)} \tag{2.45}$$

Substituting Eq.(2.44) into Eq.(2.42), the sound power radiated by a single mode is thus

$$\overline{W}_{mn} = \frac{\rho c \overline{|u_{mn}|^2}}{8\pi^2 k^2} \int_{-1}^{1} \int_{-\sqrt{1-\alpha^2}}^{\sqrt{1-\alpha^2}} \Lambda^2 \frac{(\Gamma^2 + \Pi^2)}{(1-\alpha^2-\beta^2)^{1/2}} \, d\beta \, d\alpha \tag{2.46}$$

where $\Gamma = (\varepsilon\gamma - \vartheta\varsigma)$ and $\Pi = (\vartheta\gamma + \varepsilon\varsigma)$. Because only spectral components of $\widetilde{V}_{mn}$ with $\alpha^2+\beta^2 \leq 1$ can radiate sound to the far field, the integrands over α and β are calculated for the area of non-dimensional wavenumber space enclosed by a circle of unit radius centred on the origin.

From Eq.(2.17), as $\overline{< |u_{mn}^2| >}$ equals $\overline{|u_{mn}^2|}/8$, the modal radiation efficiency is

$$\sigma_{mn} = \frac{1}{\pi^2 (ka)(kb)} \int_{-1}^{1} \int_{-\sqrt{1-\alpha^2}}^{\sqrt{1-\alpha^2}} \Lambda^2 \frac{(\Gamma^2 + \Pi^2)}{(1-\alpha^2-\beta^2)^{1/2}} \, d\beta \, d\alpha \tag{2.47}$$

2.2.2 Singularity solution

A singularity problem occurs when the values of sample points over α and β coincide with the radiation circle $\alpha^2+\beta^2 = 1$ or $k_x^2+k_y^2 = k^2$. Although not rigorous the following approach is found to give reasonable results. If $k_p^2 = k_x^2 + k_y^2$, the infinity when $k_p = k$ can be avoided by taking the sample points in the middle of rectangular integration segments of length dk_p (see Figure 2.4). Thus in the calculation of the double integral in Eq.(2.47), this is implemented by selecting suitable sample spacing $d\alpha$ and $d\beta$.

Of course, the spacing samples must be chosen sufficiently small to obtain such a smooth graph, especially to ensure that the radiation efficiency converges to unity above the critical frequency. Figure 2.5 shows the results for the same plate dimensions as those in the previous section with $d\alpha = d\beta = 0.20, 0.15, 0.09, 0.05$ m. It shows that the radiation

where

$$k_z = (k^2 - k_x^2 - k_y^2)^{1/2}, \quad k^2 \geq k_x^2 + k_y^2$$

$$= i(k_x^2 + k_y^2 - k^2)^{1/2}, \quad k^2 \leq k_x^2 + k_y^2$$

From a knowledge of $v(x, y)$, a process of calculating $p(x, y, d)$ using the FFT can be performed as follows:

1. Calculate the discrete Fourier transform (DFT) using the two-dimensional FFT algorithm of $v(x, y)$ to obtain $\widetilde{V}_D(k_x, k_y)$.
2. Calculate $\widetilde{H}(k_x, k_y, d)$ from Eq.(2.51).
3. Multiply results of (a) and (b).
4. Calculate the inverse DFT of result (c).

The velocity $v(x, y)$ is defined on every point of a baffle having a length and width of L. The points are sampled with the spacing sample of a_s. The plate itself occupies a region in the centre of this baffle as can be seen in Figure 2.6. The velocity on the rest of the baffle is zero. However due to the truncation of the FFT, the region beyond that shown in Figure 2.6 is effectively periodic. This produces so-called replicated sources. Thus L must be chosen sufficiently large to prevent overlapping the pressure field $p(x, y)$ with that from the replicated sources causing a bias error in the analysis.

The two-dimensional DFT of $v(x, y)$ can be written as

$$\widetilde{V}_D(r\Delta k, s\Delta k) = a_s^2 \sum_{p=-N/2}^{N/2-1} \sum_{q=-N/2}^{N/2-1} v(pa_s, qa_s) e^{-j2\pi(rp+sq)/N} \tag{2.52}$$

where $N = L/a_s$ and $\Delta k = 2\pi/L$.

2.3.2 Modified Green's function

From Eq.(2.51) it can be seen that the Green's function $\widetilde{G}(k_x, k_y, d)$ becomes infinite when $k_z = 0$ although the integral is finite. To avoid another bias error in the resulting

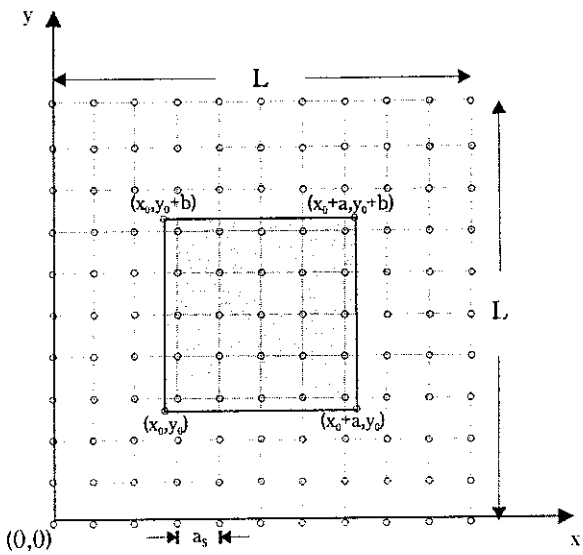

FIGURE 2.6: Diagram of a plate in a sampled baffle for sound radiation calculation using the FFT.

integral, the averaged Green's function $\overline{\widetilde{G}}$ over an annulus $k_1 \leq k_0 \leq k_2$ is introduced [5]. For $d = 0$, this yields

$$\begin{aligned}
\overline{\widetilde{G}} &= \frac{-2j[(k^2 - k_1^2)^{1/2} - (k^2 - k_2^2)^{1/2}]}{(k_2^2 - k_1^2)}, \quad k_2 \leq k, \\
&= \frac{-2j(k^2 - k_1^2)^{1/2} + 2(k^2 - k_2^2)^{1/2}}{(k_2^2 - k_1^2)}, \quad k_1 \leq k \leq k_2, \\
&= \frac{2[(k^2 - k_1^2)^{1/2} - (k^2 - k_2^2)^{1/2}]}{(k_2^2 - k_1^2)}, \quad k \leq k_1, \\
&= \frac{-j}{k}, \quad k_0 = 0,
\end{aligned} \tag{2.53}$$

where $k_1 = k_0 - \Delta k/2$, $k_2 = k_0 + \Delta k/2$ and $k_0 = (p^2 + q^2)^{1/2}\Delta k$.

Therefore $\widetilde{G}$ from Eq.(2.51) is now replaced with $\overline{\widetilde{G}}$ from Eq.(2.53). Substituting this into Eq.(2.50), the acoustic pressure on the source plane ($d = 0$) is now

$$p(x, y, 0) = j\omega\rho \boldsymbol{F}^{-1}[\widetilde{V}_D(k_x, k_y)\overline{\widetilde{G}}(k_x, k_y, d)] \tag{2.54}$$

Finally, the power radiated by the plate can be calculated in the spatial domain, given by

[2] In Williams [5], a typing mistake is made on the operator of the denominator, i.e. $k_2^2 + k_1^2$.

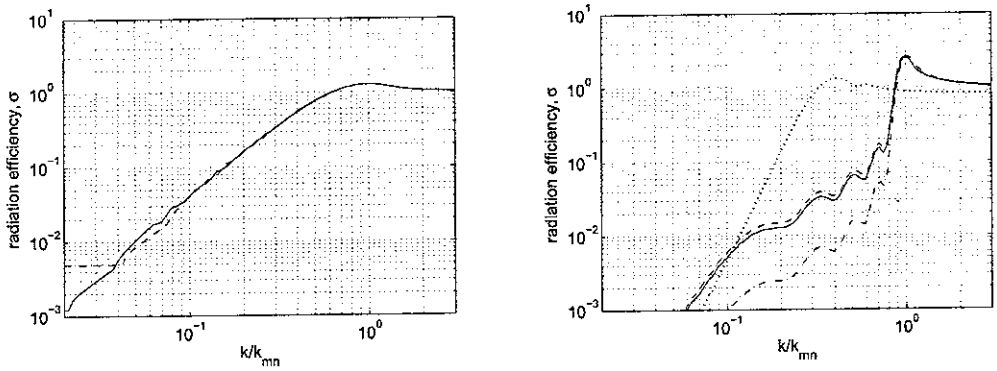

FIGURE 2.7: Radiation efficiency of a simply supported baffled plate using various FFT points. (a) mode (1,1): $L = 6.4$ m, $a_s = 0.1$ m (– –); $L = 12.8$ m, $a_s = 0.1$ m (—) and (b) mode (10,1): $L = 6.4$ m; $a_s = 0.1$ m ($\cdots$), $a_s = 0.05$ m (– · –), $a_s = 0.04$ m (– –), $a_s = 0.03$ m (—).

$$W = \frac{1}{2}\int_0^L \int_0^L \Re[p(x,y,0)]v(x,y)\,dx\,dy \tag{2.55}$$

since $v(x,y)$ is real. Alternatively, in the wavenumber domain, the sound radiation power is given by

$$W = \frac{1}{2}\int_0^k \int_0^{\sqrt{k^2-k_y^2}} \Re[\widetilde{P}^*(k_x,k_y)\widetilde{V}_D(k_x,k_y)]\,dk_x\,dk_y \tag{2.56}$$

where $k_x = r\Delta k$ and $k_y = s\Delta k$ and * denotes the conjugate form. The wavenumbers are filtered so that only those satisfying $k_x^2 + k_y^2 < k^2$ are retained in the calculation.

The radiation efficiency can be found by applying Eq.(1.1).

Figure 2.7 presents the results for modes (1,1) and (10,1) using various numbers of points in the FFT, i.e. using different baffle lengths, L and sample spacing, a_s. From Figure 2.7(a), using $L = 6.4$ m and $a_s = 0.1$ m, a bias error appears at low frequency. It can be seen that the error is then reduced by using larger values of L (larger baffle).

For the higher mode, the bias error is very small at low frequency and is not shown in the plot. However, without changing the baffle length, a finer resolution of sample points is required to obtain the true result of the radiation efficiency. This can be explained as follows. In mode (10,1), there are 5 structural wavelengths in the plate length L. In this case $L = 0.65$ m is used, therefore $\lambda = 0.65/5 = 0.13$ m. Meanwhile more than two

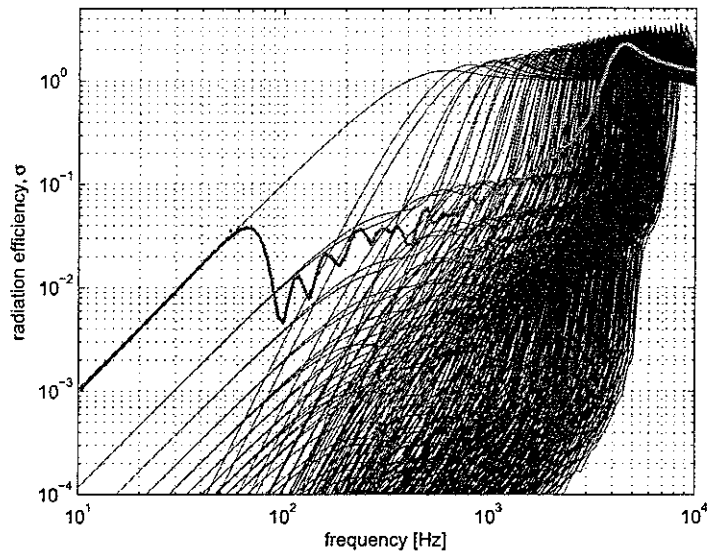

FIGURE 2.8: Modal and average radiation efficiency of a simply supported rectangular baffled plate ($0.65 \times 0.5 \times 0.003$ m aluminium plate with $\eta = 0.1$) using wavenumber decomposition:—, modal radiation efficiency; ——, average radiation efficiency.

points are required to represent one wavelength digitally. Therefore the sample spacings needed are $a_s \ll 0.13/2 = 0.065$ m. Figure 2.7(b) presents the radiation efficiency using $L = 6.4$ m and different values of a_s. It is clear that for $a_s = 0.1$ m, the result does not capture the interference due to the modal pattern. For $a_s < 0.065$ m, the results converge to the true value of radiation efficiency as the resolution of the sample spacing gets finer. It appears that 3 or more points per wavelength are required.

2.4 Comparison of the baffled methods

2.4.1 Example results

A comparison is made of the above methods by applying them to calculate the average radiation efficiency of a rectangular plate having dimensions of $0.65 \times 0.5 \times 0.003$ m, density 2700 kg/m^3, Young's modulus 7×10^{10} N/m^2, and damping loss factor 0.1. The frequency resolution is 40 points per decade, spaced logarithmically.

Figure 2.8 presents the modal and average radiation efficiency calculated using the wavenumber domain approach. The spatial domain approach gives identical results hence these are not presented here. It can be seen from the average radiation efficiency

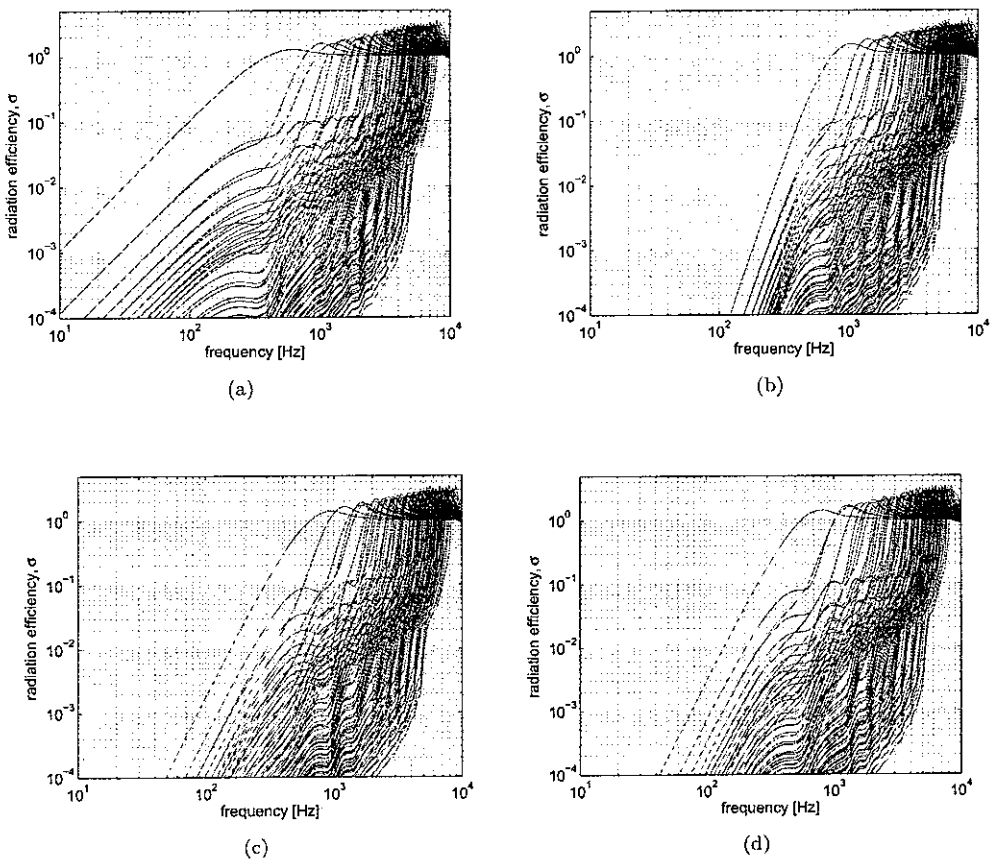

FIGURE 2.9: Self-radiation efficiency of each mode of a baffled plate: (a) odd-odd modes; (b) even-even modes; (c) odd-even modes and (d) even-odd modes.

that the overall result below 70 Hz depends on the first mode (mode (1,1)). The velocity of the plate shown below (see Figure 2.11) indicates that the first mode dominates the response in this region, and moreover it has the highest modal radiation efficiency. Above 70 Hz, the average radiation efficiency suddenly drops and then rises gradually until it reaches the maximum at about 4 kHz. This peak at about 4 kHz is the critical frequency, i.e. $f_c = (\rho_s h/B)^{1/2} c^2/2\pi$ where ρ_s is the density, h is the thickness and B is the bending stiffness of the plate. For the plate thickness considered, 3 mm, the critical frequency is 4022 Hz.

Figure 2.9 shows the modal radiation efficiencies of modes, separated into odd-odd, even-even, odd-even and even-odd modes. From Figure 2.8, the slope of the average radiation efficiency at frequencies below 70 Hz is 20 dB/decade. It can be seen that it corresponds to the slope for the odd-odd modes where the first mode is dominant.

Acting like monopole sources, the odd-odd modes are the highest mode contributing to the sound radiation, see Figure 2.9(a). The even-odd and the odd-even modes, with 40 dB/decade slope, act like dipole sources. They radiate sound less effectively than the odd-odd modes, see Figure 2.9(c) and (d). Meanwhile the even-even modes resemble a quadrupole source behaviour. They are the smallest modes in the sound radiation with a slope of 60 dB/decade, see Figure 2.9(b).

It is interesting to note that these slopes apply at low frequencies up to around 300 Hz. Above 300 Hz, where the width of the plate (0.5 m) is greater than half an acoustic wavelength, the curves are more complex due to interference effects before rising to a peak at a frequency where the acoustic wavenumber equals the plate number in their mode.

Figure 2.10 presents the average radiation efficiency for various values of the damping loss factor. It shows that the significant effect of damping to the sound radiation lies in the frequency range between the first peak and the critical frequency. The trend of the radiation efficiency in this frequency range is dominated by the 'edge' modes ($ka \ll 1$ and $kb \ll 1$) and 'corner' modes ($ka < 1$, $kb > 1$ or $ka > 1$, $kb < 1$) [18] where the cancellation of the radiation from adjacent regions on the plate takes place. The radiation from the first mode, which has the form of a monopole source, is not affected by the damping. The radiation efficiency is also independent of the damping above the critical frequency.

The modal velocity amplitude around each resonance decreases as the damping increases, see Eq.(2.13), while the decrease of modal velocity amplitude also decreases the spatially average velocity. With higher damping, waves propagating from the force point decay faster so that the effect of the nearfield close to the force point has a greater importance than the contribution of resonant modes [18].

It also can be seen that the trend has considerable fluctuation at low frequency and gets smoother as the frequency increases. This can be related to how many modes contribute in the frequency range of interest. This can be investigated from the response of the plate shown in Figure 2.11. The modes can be still differentiated at low frequecies (up to about 300 Hz), but at high frequencies, the modes are very dense so that the average response becomes almost a smooth curve. The modal density $n(\omega)$ determines the number of modes in a unit frequency band. For bending waves on a plate, it is

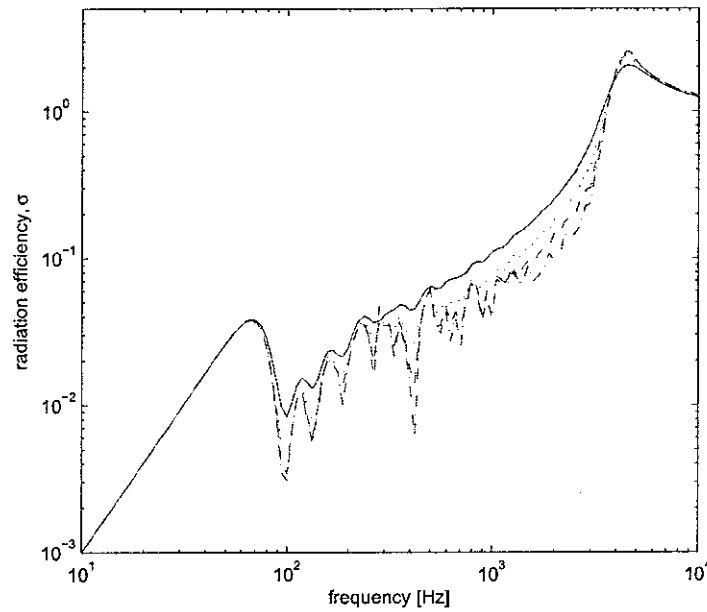

FIGURE 2.10: The average radiation efficiency of a baffled plate with different damping loss factor: —, 0.2; $\cdots$, 0.1; – –, 0.05; – $\cdot$ –, 0.01

independent of frequency and is given by [17]

$$n(\omega) = 0.276\frac{S}{hc_L} \tag{2.57}$$

where S is the plate area, h is the plate thickness and $c_L = \sqrt{E/\rho_s(1-\nu^2)}$ is the longitudinal wavespeed in the plate. The modal overlap factor is given by

$$MOF = n(\omega)\omega\eta \tag{2.58}$$

where η is the damping loss factor. This is shown in Figure 2.12 for $\eta = 0.1$. This indicates that MOF=1 occurs at around 300 Hz. At high frequency, where MOF$\gg$1, the contribution of single modes is of interest than the average over several modes. In Figure 2.10 it can be seen that the radiation efficiency curves become more smooth above 300 Hz for $\eta = 0.2$, 600 Hz for $\eta = 0.1$ and 1200 Hz for $\eta = 0.05$, i.e. for MOF>2.

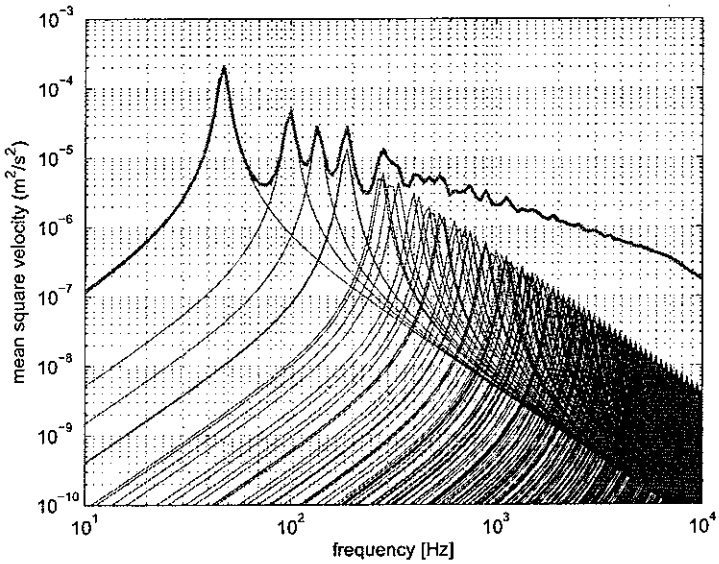

FIGURE 2.11: Contibution of modal mean square velocity (—) to total mean square velocity (—) of a rectangular plate ($0.65 \times 0.5 \times 0.003$ m aluminium plate with $\eta = 0.1$).

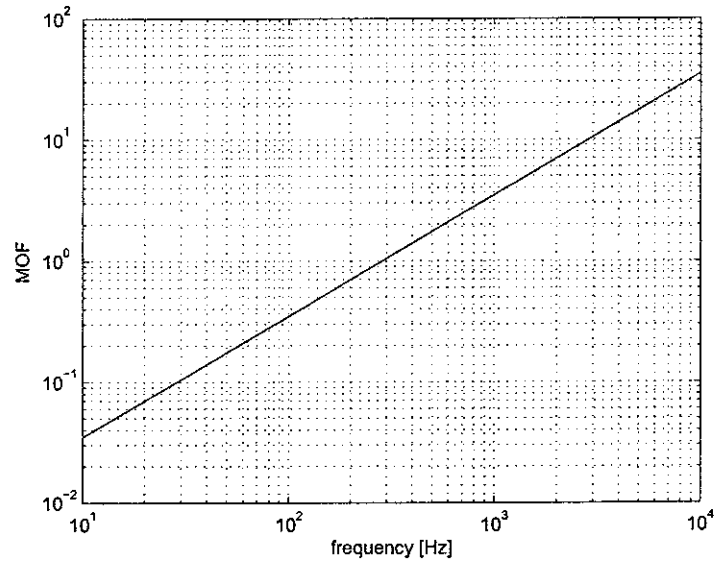

FIGURE 2.12: Modal overlap factor of the plate ($0.65 \times 0.5 \times 0.003$ m aluminium plate with $\eta = 0.1$).

2.4.2 Calculation time

Considering Eq.(2.20) in the spatial domain approach, the modal radiation is calculated by integrating over a hemisphere of farfield positions. Using the wavenumber domain scheme, the radiation efficiency is found directly for each wavenumber, but integration is then performed over wavenumber components which contribute to the radiated sound. This method can also be used to plot the spectrum of the plate velocity [18] as a function of wavenumber. This gives a better insight into the mechanism of sound radiation.

Both methods involve double layer integrals. However in the spatial approach, the calculation has to deal with integrating factors of the form of $\sin(\sin(A)\cos(B))$ as expressed in Eq.(2.7), Eq.(2.20) and (2.21). To obtain a good accuracy of result, this form must be solved with a good resolution of integration segments. Consequently, this increases the calculation time. On the other hand in the wavenumber domain approach, the equation has been performed more efficiently as the integration only employs the multiplication of the form of $\sin(A)$ or $\sin(B)$ (see Eq.(2.47)). A sufficient resolution, not necessarily as good as that in the spatial domain, can save significant amount of the calculation time. Using MATLAB on a personal computer Pentium 4® 0.99 GB RAM, the calculation using the wavenumber domain approach with $d\alpha = d\beta = 0.03$ based on 400 modes takes approximately 8 minutes. For the spatial domain approach, to have a good convergence at high frequencies up to 10 kHz, the error tolerance needed is 10^{-9}. With the same number of modes, the calculation of the radiation efficiency takes more than 4 hours.

Despite the advantages of the FFT algorithm, the FFT approach is not found to be an efficient method as this technique is not a direct method to calculate the radiation efficiency. It is time consuming as the averaged Green's function $\overline{\overline{G}}$ needs to be constructed first before implementing the inverse FFT of the plate velocity for each frequency, and later calculating the acoustic power. As described in section 2.3, an accurate result needs good resolution of sample points and a larger baffle is required to overcome the bias error at low frequency, especially in the first mode. The calculation of a single modal radiation efficiency for 64×64 points FFT takes 11 seconds. The equivalent calculation is estimated to take more than 15 hours for the average over all modes. Therefore, the calculation of the averaged radiation efficiency using this method is not encouraged here.

Chapter 3

Radiation efficiency of an unbaffled plate

3.1 Iterative scheme using the FFT

3.1.1 Algorithm

Continuing the FFT method for calculating the sound radiation for baffled plates, Williams [9] also developed this for application to unbaffled, finite plates. This involves using an iterative scheme where Rayleigh's integral and its inverse are written in the wavenumber domain. The FFT algorithm is then implemented to evaluate them.

Applying the averaged Green's function used in the baffled plate calculation in section 2.3, Eq.(2.54) gives Rayleigh's integral formula as

$$p(x,y,0) = j\omega\rho \boldsymbol{F}^{-1}[\widetilde{V}(k_x,k_y)\overline{\widetilde{G}}(k_x,k_y,0)] \tag{3.1}$$

Inverting Eq.(3.1) gives

$$v(x,y) = -(j/\omega\rho)\boldsymbol{F}^{-1}[\widetilde{P}(k_x,k_y)/\overline{\widetilde{G}}(k_x,k_y,0)] \tag{3.2}$$

In the case of a baffled plate, the velocity is defined on the plate and is zero on the baffle. This velocity is then used to define the pressure everywhere. For an unbaffled

plate, neither the velocity nor the pressure are fully known and therefore an iterative procedure is employed. The velocity is used to estimate the pressure on the plate, and the pressure is then used to calculate the velocity beyond the plate. Eq.(3.1) and (3.2) are the basic formulae used in the iteration process.

Assuming P is the plate region and E is the exterior region in the plane of the plate, the mixed boundary condition for the unbaffled plate is $v(x,y) = v_i(x,y)$ on P and $p(x,y,0) = 0$ on E, where $v_i(x,y)$ is the given velocity. Note that in the FFT method, E is only defined over an aperture of dimensions $L \times L$.

The following iteration algorithm is used:

1. Start with the boundary condition for the baffled plate, i.e. $v(x,y) = v_i(x,y)$ on P and $v(x,y) = 0$ on E on the plane at $z = 0$. For a simply supported plate, Eq.(2.3) is used for $v_i(x,y)$. Implement the two dimensional FFT to find $\widetilde{V}(k_x, k_y)$ (see section 2.3).

2. Use Eq.(3.1) to obtain $p(x,y,0)$. Retain this solution for P but set $p(x,y,0) = 0$ on E.

3. Find $\widetilde{P}(k_x, k_y)$ using the FFT and calculate the new $v(x,y)$ for the whole plane at $z = 0$ from Eq.(3.2).

4. Check the mean square error of the reconstructed velocity field from

$$\epsilon = \sum_{0}^{N} \mid [v(x,y) - v_i(x,y)] \mid^2 /N \tag{3.3}$$

   where N is the total number of points considered on the plate region P.

5. If the root mean square error (RMSE) is more than a certain tolerance, the iteration is repeated from the first step by setting $v(x,y) = v_i(x,y)$ on P and leaving $v(x,y)$ unchanged on E.

When the iteration is stopped, the boundary condition in the exterior region E, $p(x,y,0) = 0$ should also be closely achieved. Williams [9] found that for RMSE less than 0.005, for a unit maximum amplitude of $v_i(x,y)$, the pressure magnitude on E was generally three orders of magnitude below its maximum value on P.

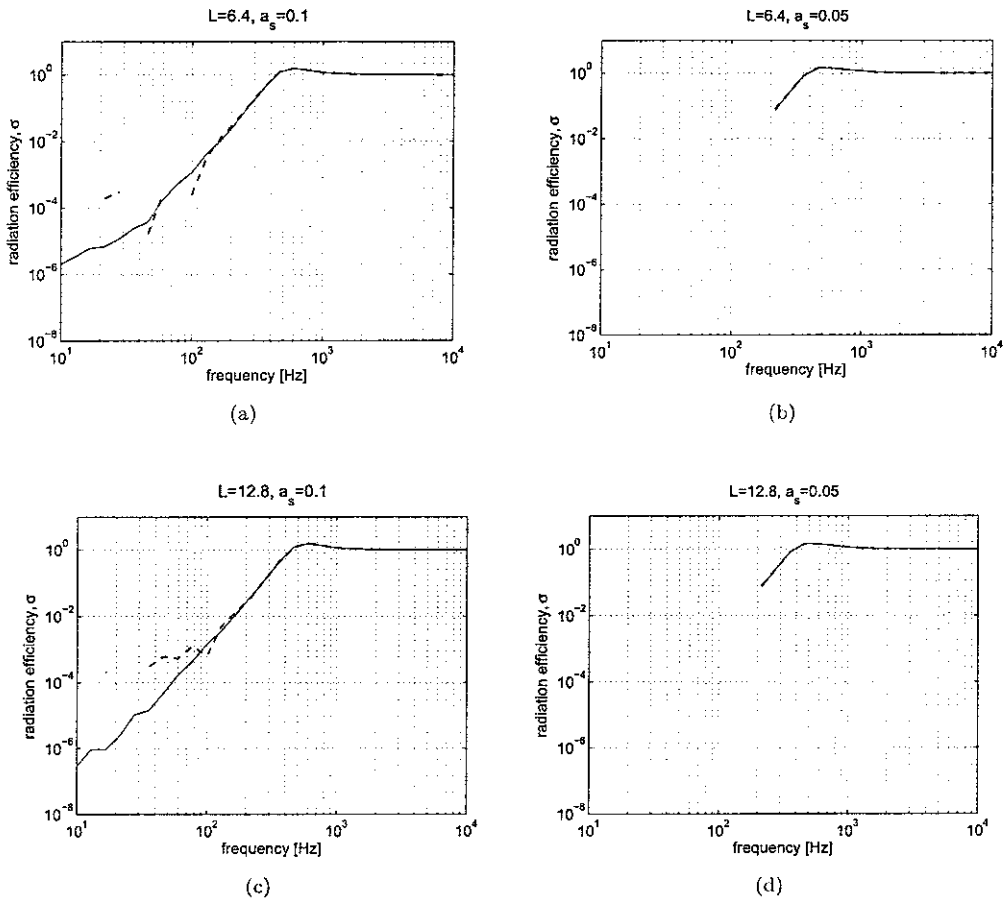

FIGURE 3.1: Radiation efficiency of mode (1,1) of a simply supported unbaffled plate using the FFT method ($0.65 \times 0.5 \times 0.03$ m aluminium plate with $\eta = 0.1$): ——, spatial domain; —, wavenumber domain.

Equivalent approaches of calculating the radiated power as those used for of the baffled plates can be employed, either by integrating over the spatial domain or over the wavenumber domain using Eq.(2.55) or Eq.(2.56) respectively.

3.1.2 Convergence problem

Figure 3.1 plots the radiation efficiency of mode (1,1) using both approaches (spatial and wavenumber domains) to calculate the radiated power (Eq.(2.55) and Eq.(2.56)) for a plate having the same dimensions and properties as in the previous sections. From Figure 3.1(a) and (c), it can be seen that using the spatial domain, the calculation results in a discontinuity below 100 Hz. Some results are actually negative. This limitation of using the spatial domain could be because the calculation includes all the wavenumbers,

of which those outside the radiation circle that contribute to the non-propagating waves may not cancel each other at low frequencies due to numerical inaccuracies. Meanwhile, results are obtained over the whole frequency range using the wavenumber domain for $a_s = 0.1$ m, but the slope of the graph deviates below 50 Hz for $L = 6.4$ m. This is due to bias error from the replicated sources (outside the window $L \times L$) as explained in section 2.3.1. This can be overcome by having a larger aperture i.e. in this case L is increased to 12.8 m, see Figure 3.1(c).

Convergence problems appear due to the sample spacing a_s used. It is found that using $a_s \leq 0.05$ m, the results for both values of L fail to converge below 200 Hz as seen in Figure 3.1(b) and (d). This might be due to the pressure discontinuity at the plate's edge. In fact, for an unbaffled disc of radius a, Williams [9] found that the mean square error did not converge for $ka < 1.7$. The results shown here suggest that it is connected with the sample spacing a_s rather than the size of the radiating plate. Unfortunately finer resolution is required to represent higher order modes so that it appears that this iterative FFT method cannot cope with higher order plate modes.

3.2 Wavenumber domain using modal basis

Laulagnet [8] has proposed a numerical evaluation for calculating sound radiation from a simply supported unbaffled plate where the pressure jump and the plate displacement are developed as a sum over the plate modes.

3.2.1 Derivation of equations

Consider a flat thin unbaffled plate with a surface area S_p located in an infinite medium, excited by a harmonic force distribution $F(x, y)$ of angular frequency ω. $\Delta p(x, y)$ is the difference of the acoustic surface pressure, thus the pressure jump at the plate's edge due to the transverse motion, given by

$$\Delta p(x, y) = p^-(x, y) - p^+(x, y) \tag{3.4}$$

where $p^-(x, y)$ and $p^+(x, y)$ are the surface pressure on the z axis at $z = 0_-$ and $z = 0_+$ respectively.

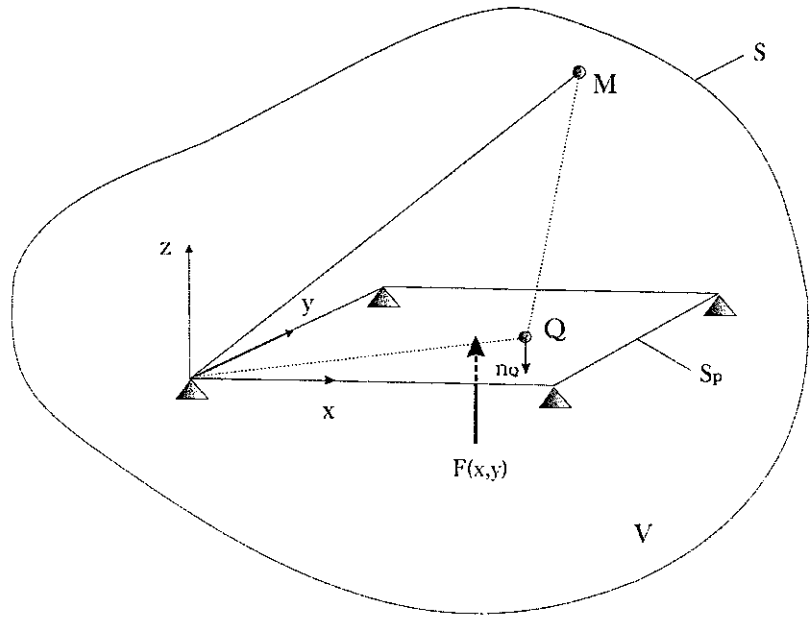

FIGURE 3.2: A simply supported plate enclosed by a volume V in the medium with its bounding surface S.

The force distribution is assumed to act normal to the plate. One can apply the equation of motion expressed as

$$B\nabla^4 w(x,y) - m\omega^2 w(x,y) = F(x,y) + \Delta p(x,y) \tag{3.5}$$

where B is the bending stiffness, m is the mass per unit area, $w(x,y)$ is the transverse displacement of the plate and ∇^4 is given by

$$\nabla^4 = \frac{\partial^4}{\partial x^4} + \frac{2\partial^4}{\partial x^2\,\partial y^2} + \frac{\partial^4}{\partial y^4} \tag{3.6}$$

The pressure anywhere in the volume encompassing the plate can be found by using Green's function, see Figure 3.2. According to Kirchhoff's integral theorem, the pressure in the surrounding fluid can be expressed by

$$p(M) = \int_S \left(p(Q)\frac{\partial G(Q,M)}{\partial n_Q} - G(Q,M)\frac{\partial p}{\partial n_Q} \right) dS \tag{3.7}$$

where M denotes a point in the medium, n_Q is the normal to the total surface taken at point Q on the plate, $G(Q,M) = e^{-jkR}/4\pi R$ is the free-field Green's function with R the distance between point Q and M.

The Green's function must satisfy

$$\nabla^2 G(Q,M) + k^2 G(Q,M) = \delta(x-x_0)\delta(y-y_0)\delta(z-z_0) \tag{3.8}$$

where δ is the Dirac delta distribution, Q is at $(x,\ y,\ z)$ and M is at (x_0, y_0, z_0). By using the two dimensional spatial Fourier transform of Eq.(3.8), the Green's function can be expressed as

$$G = \frac{j}{8\pi^2}\int_{-\infty}^{\infty}\int_{-\infty}^{\infty}\frac{e^{jk_x(x-x_0)}e^{jk_y(y-y_0)}e^{jk_z(z-z_0)}}{k_z}\,dk_x\,dk_y \tag{3.9}$$

where $k_z = \sqrt{k^2 - k_x^2 - k_y^2}$.

Considering that only outgoing waves from the plate are allowed in the calculation, the surface integral in Eq.(3.7) can be reduced to S_p, i.e. the whole surface of the plate, S_{p+} and S_{p-}. The surface at infinity is neglected since it is assumed that there is no wave reflected back to the plate.

Restricting attention to the pressure at a point M above the plate (half space, $z_0 \geq 0$), by considering the normal n_Q parallel to the z-axis as illustrated in Figure 3.2, Eq.(3.7) can be decomposed as

$$\begin{aligned} p(M) = &-\int_{S_{p+}} p^+(Q)\frac{\partial G(Q,M)}{\partial z_Q}\,dS_{p+} + \int_{S_{p-}} p^-(Q)\frac{\partial G(Q,M)}{\partial z_Q}\,dS_{p-} \\ &+\int_{S_{p+}} G(Q,M)\frac{\partial p^+}{\partial z_Q}\,dS_{p+} - \int_{S_{p-}} G(Q,M)\frac{\partial p^-}{\partial z_Q}\,dS_{p-} \end{aligned} \tag{3.10}$$

where $M \in V^+$, i.e. V^+ is the half-space above the plate.

Since the gradient of the acoustic pressure is a continuous function on the plate mid-surface S_p and the plate thickness is assumed to be very small compared with its length and width, the simple layer contribution can be neglected; S_{p+} and S_{p-} become S_p. Thus from Eq.(3.10), it is obtained that

$$\int_{S_p} G(Q,M)\left(\frac{\partial p^+}{\partial z_Q} - \frac{\partial p^-}{\partial z_Q}\right)\,dS_p = 0\,, \qquad Q \in S_p \tag{3.11}$$

Therefore

$$p(M) = \int_{S_p} \Delta p \frac{\partial G(Q,M)}{\partial z_Q} \, dS_p \tag{3.12}$$

Substituting Eq.(3.5) into Eq.(3.12) yields

$$p(M) = \int_{S_p} [B\nabla^4 w(x,y) - m\omega^2 w(x,y) - F(x,y)] \frac{\partial G(Q,M)}{\partial z_Q} \, dS_p \tag{3.13}$$

where $Q \in S_p$, $M \in V^+$.

The two-unknown fields, i.e. the acoustic field $p(M)$ and the vibration of the plate $w(Q)$ in Eq.(3.13) can be related using Euler's function in the plane of the plate at z=0.

$$\begin{aligned} \frac{\partial p}{\partial z}(M)|_{z=0} &= \rho\,\omega^2 w(M) \\ &= \int_{S_p} [B\nabla^4 w(Q) - m\omega^2 w(Q) - F(Q)] \frac{\partial^2 G(Q,M)}{\partial z_Q \partial z_M} \, dS_p \end{aligned} \tag{3.14}$$

where $\partial/\partial z_Q$ and $\partial/\partial z_M$ are the derivatives at Q and M in the z direction respectively. From Eq.(3.14), a solution for the displacement w can be found by setting $Q = M$.

3.2.2 Integral solution using modal summation

The displacement can be considered as the summation of a series of plate modes. Similar to Eq.(2.3) for the velocity, the equation can be expressed as

$$w(x,y) = \sum_{m=1}^{\infty} \sum_{n=1}^{\infty} d_{mn} \varphi_{mn}(x,y) \tag{3.15}$$

where d_{mn} is the modal displacement amplitude and φ_{mn} is the associated mode shape function as in Eq.(2.4).

The same kind of modal series can also be applied for the excitation force given by

$$F(x,y) = \sum_{m=1}^{\infty} \sum_{n=1}^{\infty} F_{mn} \varphi_{mn}(x,y) \tag{3.16}$$

where F_{mn} is the generalized force for mode (m,n).

Substituting Eq.(3.15) and Eq.(3.16) into Eq.(3.14), the equation can then be written as

$$\rho\omega^2 \sum_{m=1}^{\infty}\sum_{n=1}^{\infty} d_{mn}\varphi_{mn}(x_0,y_0) = \int_{S_p} \sum_{m=1}^{\infty}\sum_{n=1}^{\infty}[m(\omega_{mn}^2-\omega^2)d_{mn} - F_{mn}]\,\varphi_{mn}(x,y)\frac{\partial^2 G}{\partial z \partial z_0}(x,x_0,y,y_0,z=z_0=0)\,dx\,dy \tag{3.17}$$

where ω_{mn} is the resonance frequency for a single mode, similar to Eq.(2.16) defined by

$$\omega_{mn} = k_{mn}^2\sqrt{\left(\frac{B}{m}\right)} \tag{3.18}$$

where k_{mn} denotes the modal wave number of mode (m,n), which for a simply supported plate is given by

$$k_{mn} = \sqrt{\left(\frac{m\pi}{a}\right)^2 + \left(\frac{n\pi}{b}\right)^2} \tag{3.19}$$

and where the modes φ_{mn} satisfy

$$B\,\nabla^4\varphi_{mn}(x,y) = m\omega_{mn}^2\varphi_{mn}(x,y) \tag{3.20}$$

If the mode shape of the simply supported plate, say φ_{pq} is defined according to Eq.(2.4), using the orthogonality relationship, one can obtain

$$\int_{S_p} \varphi_{mn}\,\varphi_{pq}\,dS_p = \frac{S_p}{4}\delta_{mp}\delta_{nq} \tag{3.21}$$

where δ is the Kronecker's delta.

Applying this to Eq.(3.17) yields

$$\rho\omega^2\frac{S_p}{4}d_{pq} = \sum_{m=1}^{\infty}\sum_{n=1}^{\infty}[m(\omega_{mn}^2-\omega^2)d_{mn} - F_{mn}]C_{pqmn} \tag{3.22}$$

where C_{pqmn} is the acoustical cross-modal coupling terms, i.e.

$$C_{pqmn} = \int_{S_p}\int_{S_p} \varphi_{pq}(x_0,y_0)\frac{\partial^2 G}{\partial z\partial z_0}(x,x_0,y,y_0,z=z_0=0)\,\varphi_{mn}(x,y)\,dx\,dx_0\,dy\,dy_0 \tag{3.23}$$

Substituting Eq.(3.9) into Eq.(3.23) and performing the two integrals over S_p yields

$$C_{pqmn} = \frac{j}{8\pi^2} \int_{-\infty}^{\infty} \int_{-\infty}^{\infty} k_z \, \widetilde{\varphi}^*_{pq}(k_x, k_y) \widetilde{\varphi}_{mn}(k_x, k_y) \, dk_x \, dk_y \tag{3.24}$$

where $\widetilde{\varphi}_{mn}(k_x, k_y)$ is the Fourier transform of the mode shape $\varphi_{mn}(x, y)$ which is expressed by

$$\widetilde{\varphi}_{mn}(k_x, k_y) = \int_0^a \int_0^b \varphi_{mn}(x, y) e^{-j(k_x x + k_y y)} \, dx \, dy \tag{3.25}$$

After evaluating analytically

$$\widetilde{\varphi}_{mn}(k_x, k_y) = \frac{ab}{\pi^2 mn} \left[\frac{(-1)^m e^{-j\mu} - 1}{(\mu/(m\pi))^2 - 1} \right] \left[\frac{(-1)^n e^{-j\chi} - 1}{(\chi/(n\pi))^2 - 1} \right] \tag{3.26}$$

where $\mu = k_x a$ and $\chi = k_y b$.

For the conjugate form of the modal shape $\varphi^*_{pq}(x, y)$, the result is identical except that the sign of the exponential is changed from negative to positive, i.e.

$$\widetilde{\varphi}^*_{pq}(k_x, k_y) = \frac{ab}{\pi^2 pq} \left[\frac{(-1)^p e^{j\mu} - 1}{(\mu/(p\pi))^2 - 1} \right] \left[\frac{(-1)^q e^{j\chi} - 1}{(\chi/(q\pi))^2 - 1} \right] \tag{3.27}$$

It can be seen that $\widetilde{\varphi}_{mn}$ or $\widetilde{\varphi}^*_{pq}$ are identical to Φ in Eq.(2.7).

From Eq.(3.25), it can be found that the integrand, with respect to k_x, is an even function when the mode orders (p,m) are of the same parity. Also, with respect to k_y, it is an even function when the mode orders (q,n) are of the same parity.

Therefore Eq.(3.24) can be simplified as

$$C_{pqmn} = \frac{j}{2\pi^2} \int_0^{\infty} \int_0^{\infty} k_z \, \widetilde{\varphi}^*_{pq}(k_x, k_y) \widetilde{\varphi}_{mn}(k_x, k_y) \, dk_x \, dk_y \tag{3.28}$$

when p and m are of the same parity and q and n are also of the same parity. The remaining cases will have $C_{pqmn} = 0$.

Finally after substituting Eq.(3.26) and Eq.(3.27) into Eq.(3.28), it is found that

$$C_{pqmn} = C_{mnpq} = \frac{2j}{pqmn} \left(\frac{ab}{\pi^3} \right)^2 \int_0^{\infty} \int_0^{\infty} k_z \Upsilon \, \Omega \, dk_x \, dk_y \tag{3.29}$$

where

$$\Upsilon = \frac{1-(-1)^p \cos\mu}{((\mu/p\pi)^2-1)((\mu/m\pi)^2-1)}, \quad \Omega = \frac{1-(-1)^q \cos\chi}{((\chi/q\pi)^2-1)((\chi/n\pi)^2-1)}.$$

In practice, the infinite limits of the double layer integrals over k_x and k_y can be limited as in [8] to

$$k_x^{max} = (1+K)\frac{p\pi}{a}, \quad k_y^{max} = (1+K)\frac{q\pi}{b} \tag{3.30}$$

for some $K \geq 1$.

To overcome the singularities in the integration, the method used in the wavenumber domain in Section 2.2.2 can be applied.

From Eq.(3.22), after numerically evaluating C_{mnpq}, the displacement modal amplitude d_{pq} can be found by solving the linear system

$$[C_{mnpq}]\{m(\omega_{pq}^2-\omega^2)d_{pq}\} - \rho\omega^2\frac{S_p}{4}[I]\{d_{pq}\} = [C_{mnpq}]\{F_{pq}\} \tag{3.31}$$

where $[C_{mnpq}]$ is the cross coupling matrix and $[I]$ is the identity matrix of size $N \times N$.

After inverting C_{mnpq} this gives

$$\{m(\omega_{pq}^2-\omega^2)d_{pq}\} - \rho\omega^2\frac{S_p}{4}[C_{mnpq}]^{-1}\{d_{pq}\} = \{F_{pq}\} \tag{3.32}$$

The influence of the fluid on the plate motion can be identified from the last term on the left-hand side, which by multiplying the term with $S_p/4$, can be written in terms of the so-called cross-modal radiation impedance $[Z_{mnpq}]$, i.e.

$$[Z_{mnpq}]\{j\omega d_{pq}\} = -\rho\omega^2\left(\frac{S_p}{4}\right)^2[C_{mnpq}]^{-1}\{d_{pq}\} \tag{3.33}$$

Therefore

$$[Z_{mnpq}] = j\omega\rho\left(\frac{S_p}{4}\right)^2[C_{mnpq}]^{-1} \tag{3.34}$$

If the matrix $[Z_{mnpq}]$ is normalized to $\rho c S_p/4$, the normalized cross-modal radiation impedance, which is the same term as the radiation efficiency, for a simply supported

unbaffled plate is then defined. It expressed as

$$[\sigma_{mnpq}] = \frac{1}{\rho c S_p/4}[Z_{mnpq}] = jk\frac{S_p}{4}[C_{mnpq}]^{-1} \tag{3.35}$$

Here, one has to invert the matrix $[C_{mnpq}]$ first. Thus $[\sigma_{mnpq}]$ strongly depends not only on the accuracy of the calculated $[C_{mnpq}]$ but also on the size of the matrix $[C_{mnpq}]$ to be inverted. In order to simplify the calculation without dealing with a matrix inversion, an approximate formula can be applied which is defined by

$$[\sigma_{pqpq}] \approx jk\frac{S_p}{4}\frac{1}{C_{pqpq}} \tag{3.36}$$

in which the off-diagonal terms in C_{mnpq} are neglected. In other words, as in the baffled plate case in section 2.1.2, only the self-modal radiation contributions are taken into account in the calculation. The effect of the cross-modal coupling is eliminated.

Laulagnet [8] showed that compared with the exact solution, the approximate one gives a very good approximation in light fluid such as air.

The radiation efficiency of the unbaffled plate takes into account the fluid loading on both sides of the plate but has been normalised only by the area of one side. To have an equivalency to the radiation efficiency of the baffled plate, as a consequence, the term $[\sigma_{pqpq}]$ has to be further divided by two.

3.3 Results and comparison with baffled plate

Figure 3.3 shows a result for a rectangular plate having the same dimensions and properties as the baffled plate described in section 2.4. It can be seen that the slope of the average radiation efficiency is 40 dB/decade at very low frequencies instead of 20 dB/decade found for the baffled plate.

With different values of damping loss factor, Figure 3.4 shows the same phenomenon as that in the baffled plate where the radiation efficiency increases as the damping increases. As explained in section 2.4, with high damping, the contributions of individual modes become less important and consequently the curves become smoother. Moreover the

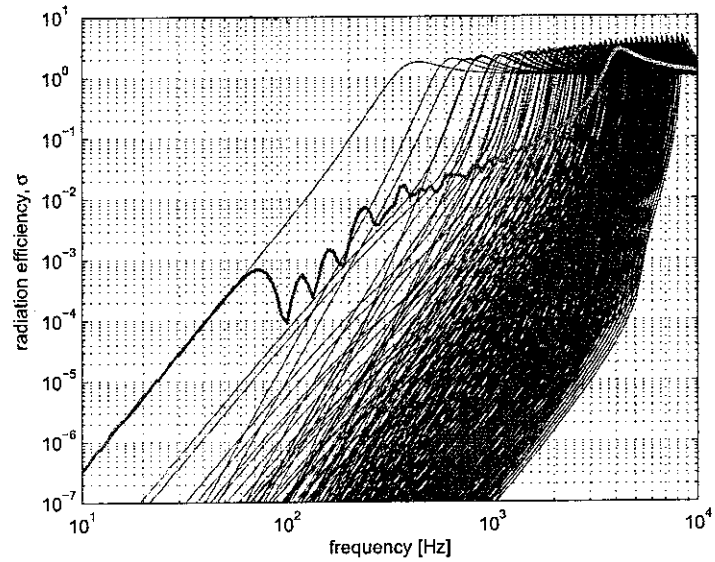

FIGURE 3.3: Modal and average radiation efficiency of a simply supported unbaffled plate ($0.65 \times 0.5 \times 0.003$ m aluminium plate with $\eta = 0.1$):—, modal radiation efficiency; ——, average radiation efficiency.

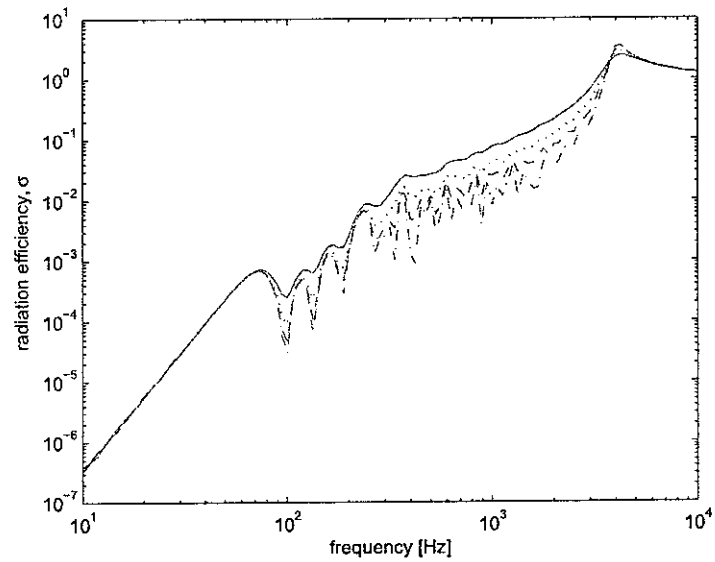

FIGURE 3.4: The average radiation efficiency of an unbaffled plate with different damping loss factor: —, 0.2; $\cdots$, 0.1; – –, 0.05; – $\cdot$ –, 0.01 (aluminium plate: $0.65 \times 0.5 \times 0.003$ m).

near-field in the vicinity of the driving point force has a greater effect, increasing the sound radiation.

Figure 3.5 compares the average radiation efficiency of the baffled and unbaffled plates. As well as the difference in slope noted at low frequency, in the region of acoustic short-circuiting between 100 and 3000 Hz, the unbaffled plate has a lower radiation efficiency

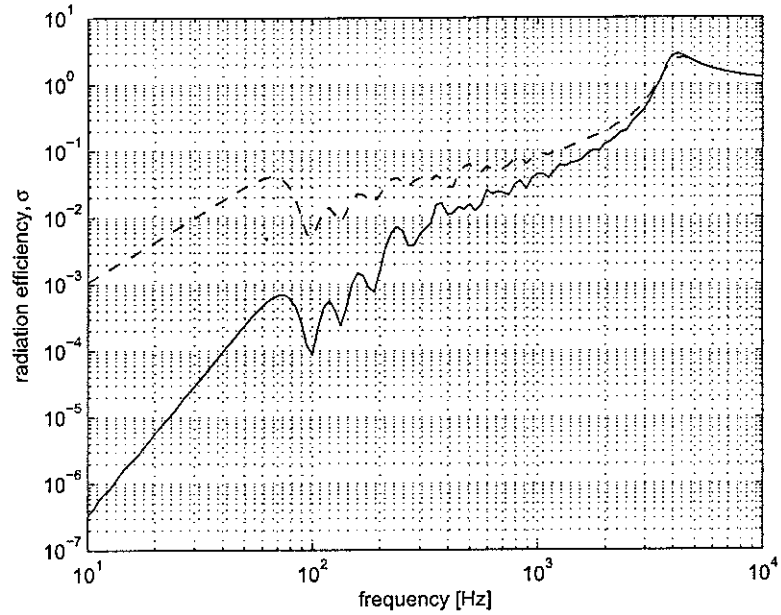

FIGURE 3.5: Comparison of average radiation efficiency between unbaffled (—) and baffled (– –) plates ($0.65 \times 0.5 \times 0.003$ m aluminium plate with $\eta = 0.1$).

than that of the baffled plate. Without the baffle, the plate becomes an ineffective radiator at low frequencies where the wave cancellation phenomenon is more efficient due to the short circuit effect from one side of the plate to the other. It is shown that in this region, the frequency dependance is approximately 10 dB/decade for the baffle plate and 20 dB/decade for the unbaffled plate.

Using the same personal computer specification as in the baffled plate (Section 2.4.2) with $K = 1$, $dk_x = 2\pi a/dn$ and $dk_y = 2\pi b/dn$ for $dn = 40$, the calculation of the averaged radiation efficiency takes approximately 4 hours.

The ratio between the radiation efficiencies of unbaffled and baffled plates is presented in a dB difference in Figure 3.6 for various plate dimensions.

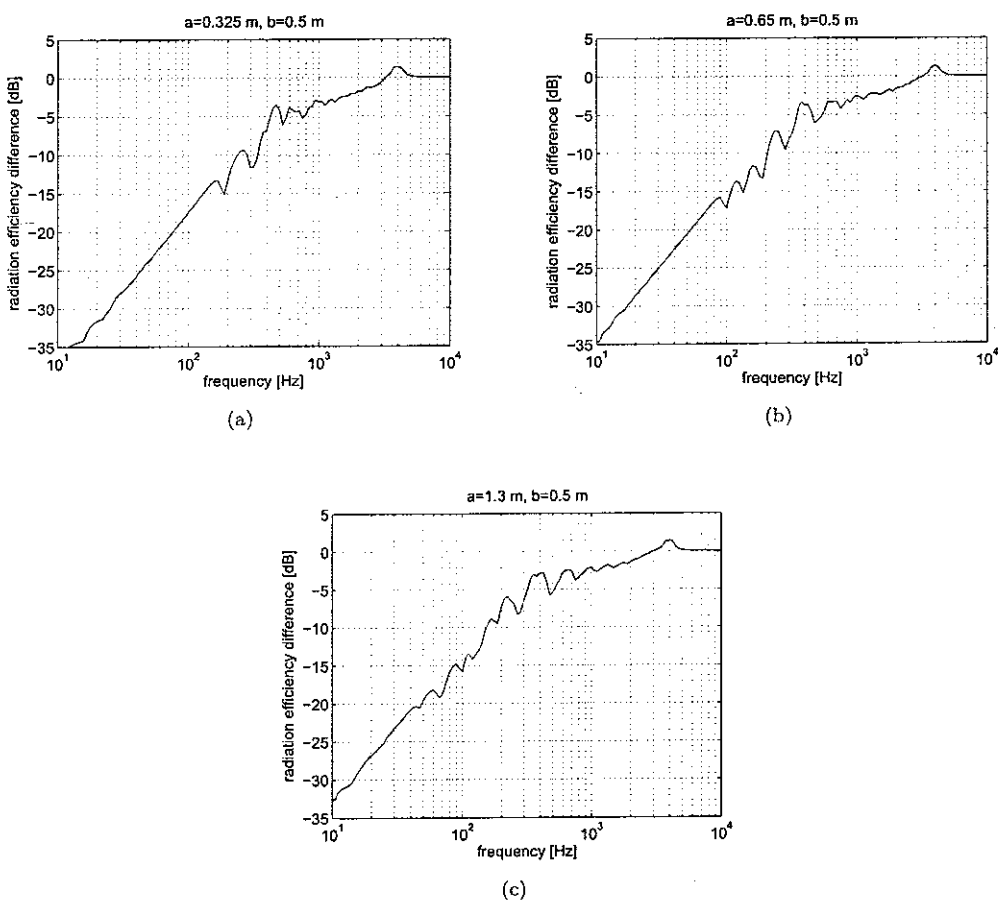

FIGURE 3.6: Ratio between radiation efficiencies of unbaffled and baffled plates presented as a dB difference for plates with various dimensions.

Chapter 4

Radiation efficiency from a single point force position

In the previous chapters, the average radiation efficiency of a simply supported plate was obtained from the summation over the modes. This method has the advantage that information is provided about the contribution of the various modes to the sound radiation. Moreover no account is needed of the cross-modal radiation. However, it does not correspond to a practical situation since the result is averaged over all point force positions on the plate.

In this section the distribution of the radiation efficiencies from several single point force positions is studied for a baffled plate.

The method is explained as follows. The velocity of the plate $v(x,y)$ due to a single point force position at a location (x_0, y_0) can be calculated as a sum of modes. Recalling Eq.(2.3), the expression is given by

$$v(x,y) = \sum_{m=1}^{\infty} \sum_{n=1}^{\infty} u_{mn} \varphi_{mn}(x,y) \tag{4.1}$$

where φ_{mn} is the mode shape function from Eq.(2.4) and u_{mn} is the complex velocity amplitude of the mode from Eq.(2.13).

The velocity in the wavenumber domain $\widetilde{V}(k_x, k_y)$ is then obtained by applying the two-dimensional FFT to $v(x,y)$. Therefore for each frequency, the FFT method for a simply

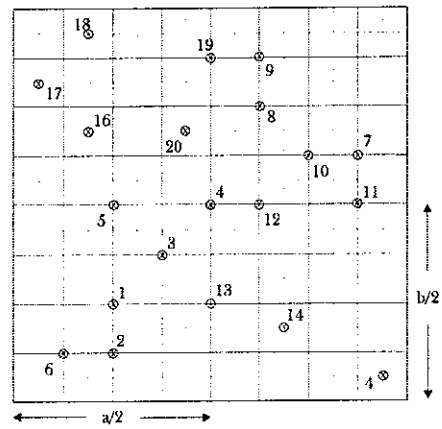

FIGURE 4.1: Samples of point force position on the plate.

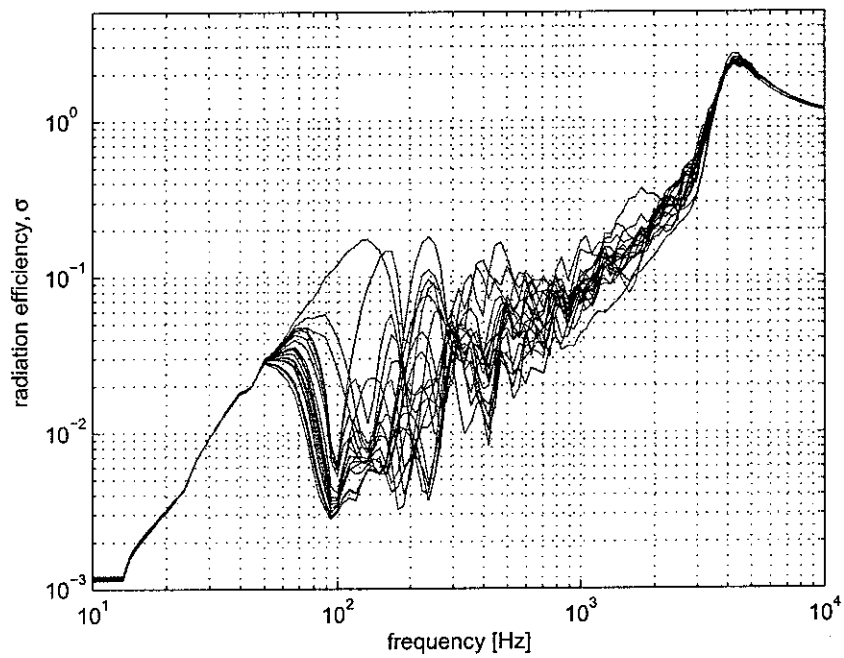

FIGURE 4.2: Distribution of radiation efficiency over 20 point force positions on plate ($0.65 \times 0.5 \times 0.003$ m aluminium plate with $\eta = 0.1$).

supported baffled plate described in section 2.3 can be implemented, but now it is for the total velocity at each frequency, not on a mode-by-mode basis.

For an example result, 20 points are selected scattered over on the plate's surface as shown in Figure 4.1. The plate dimensions and properties are still the same as those in the previous chapters. In the FFT method, the baffle length $L = 12.8$ m and the spacing sample $a_s = 0.03$ m are used. The radiation efficiencies obtained are plotted together in Figure 4.2.

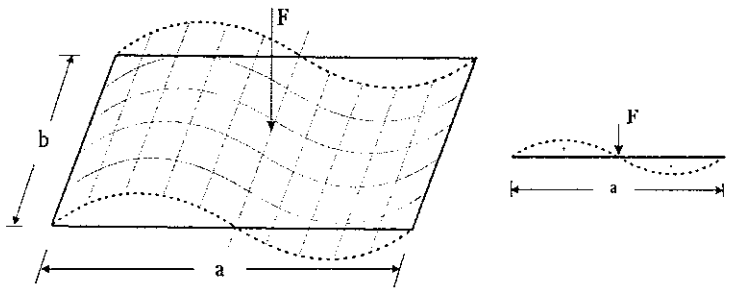

FIGURE 4.3: Excitation at the node point of mode (2,1).

The results show the same trend as that of the average radiation efficiency, see Figure 2.8. It reveals that the radiation efficiencies from different point force positions only vary between about 50 Hz and the critical frequency around 4 kHz, i.e. mainly in the corner and edge mode regions. As these regions are the focus of observation, the bias error clearly seen at very low frequency due to the application of the FFT method can be ignored. It is also interesting to see that some high peaks appear in the variation. These peaks show that certain modes become dominant due to the absence of other certain modes. For instance from Figure 4.2, the radiation efficiency having the highest peak at around 140 Hz is obtained when the point force is applied at the middle of the plate (point No.4). The excitation at the middle of the plate does not generate modes (2,1) or (1,2) because the force is applied exactly at the node point of the modes, see Figure 4.3. Mode (1,1) then becomes dominant over a wider frequency range leading to a higher overall radiation efficiency.

Figure 4.4 shows the range of the variation corresponding to the 10% and 90% bands at each frequency in narrow band and also in 1/3-octave band, arranged with the increasing damping ($\eta = 0.05$, $\eta = 0.1$ and $\eta = 0.2$) to see the variation with different damping loss factor. As seen in the figure, the average radiation efficiency (calculated directly using the wavenumber domain method) lies among the variations. It can be seen that there is no significant change appears in the extent of the variation except at few specific frequencies.

Figure 4.5 shows the range between the 10% and 90% curves, now plotted in dB (10 $\log_{10} \sigma$). Around the peaks at 160 Hz and 230 Hz, the variation increases with reducing damping, but above 300 Hz there is no consistent effect of damping. These phenomena can be clearly seen in 1/3-octave band in Figure 4.6. The consistent damping effect is only between 160 Hz and 230 Hz. Figure 4.7 shows the averaged and 10/90 percentile

curves of the radiation efficiency for three different plate dimensions.

From Figure 4.4, one can see the dip at 100 Hz in the average result is relatively close to the minimum range of the variation (10 percentile). The same phenomena also appears in each case in Figure 4.7. This dip corresponds to the natural frequency of the first even-odd mode (2,1), see Figure 2.11. The peaks in the variability in Figure 4.5 corresponds to the dips in the mean-square velocity, not to resonances (see Figure 2.11). On the contrary, one can note that the dips in the variability, especially up to 300 Hz, correspond to the resonances. This means that the averaged radiation efficiency can be better estimated from any point force positions at the plate resonances.

The variation of the radiation efficiency also does not change significantly with the plate dimension. As seen in Figure 4.7, only some peaks are developed and or shifted depending on the point force position relative to the plate surface. Figure 4.8 shows that the trend of the variability is still the same for different plate dimensions. At low frequencies the results are influenced by the errors from the FFT method when calculating the radiation efficiency.

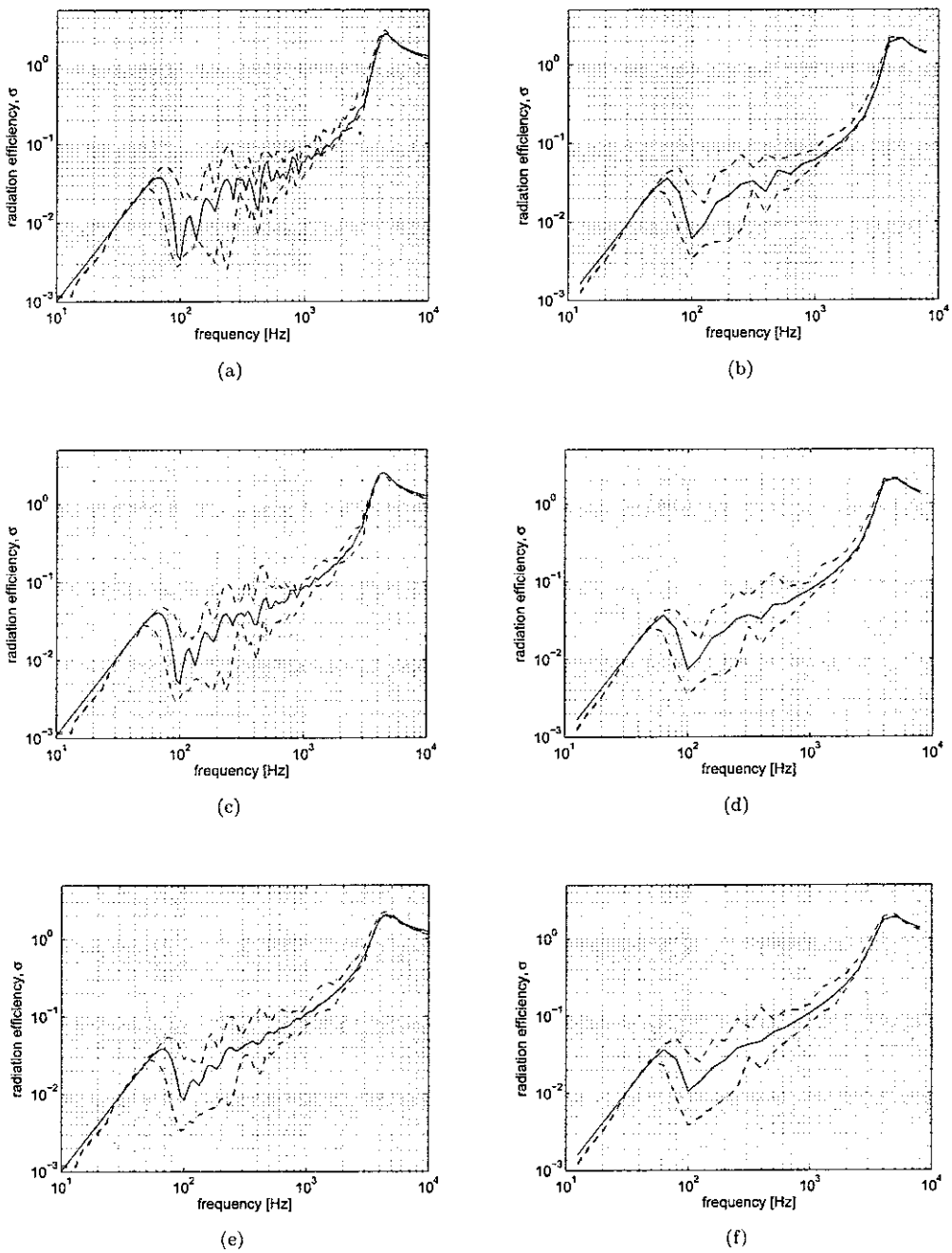

FIGURE 4.4: Range of radiation efficiency variation using 10/90 percentiles (−−) and average radiation efficiency (—) in narrow band (left side) and 1/3-octave band (right side) (0.65 × 0.5 × 0.03 m aluminium plate with: (a)-(b). $\eta = 0.05$, (c)-(d). $\eta = 0.1$, (e)-(f). $\eta = 0.2$).

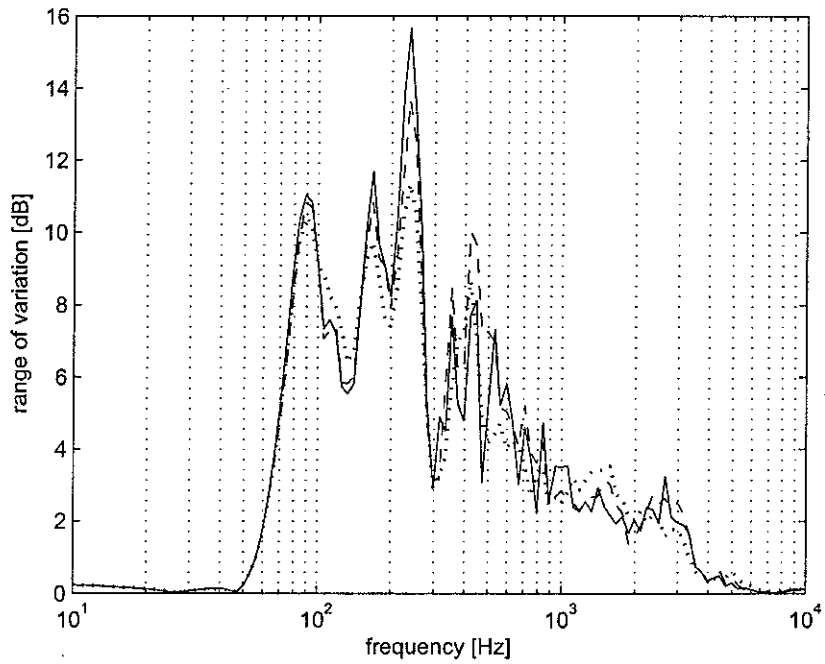

FIGURE 4.5: Variability of radiation efficiency from 10/90 percentiles (0.65 × 0.5 × 0.03 m aluminium plate): $\eta = 0.05$ (—); $\eta = 0.1$ (−−); $\eta = 0.2$ (···).

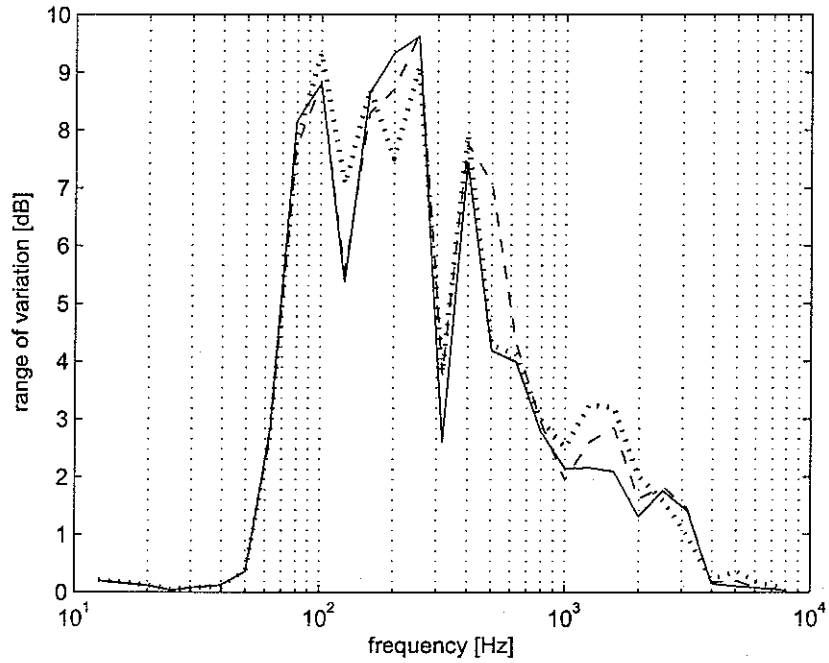

FIGURE 4.6: Variability of radiation efficiency from 10/90 percentiles in 1/3 octave band (aluminium plate: 0.65 × 0.5 × 0.03 m.): $\eta = 0.05$ (—); $\eta = 0.1$ (−−); $\eta = 0.2$ (···).

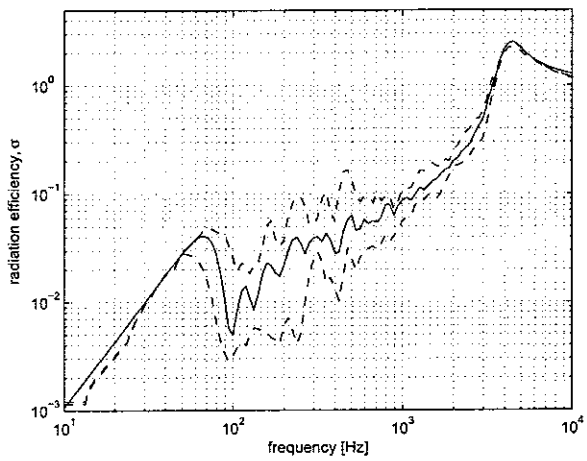

(a)

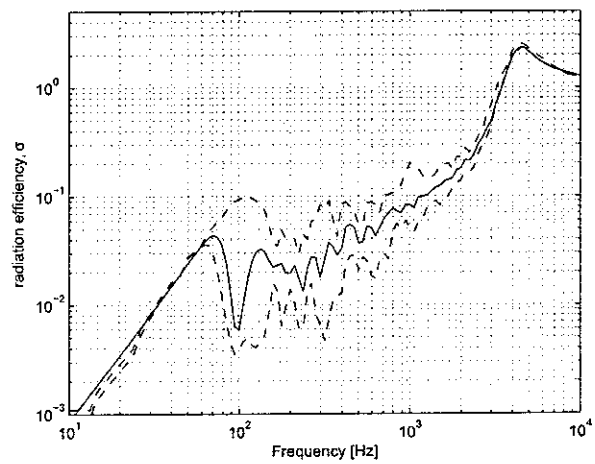

(b)

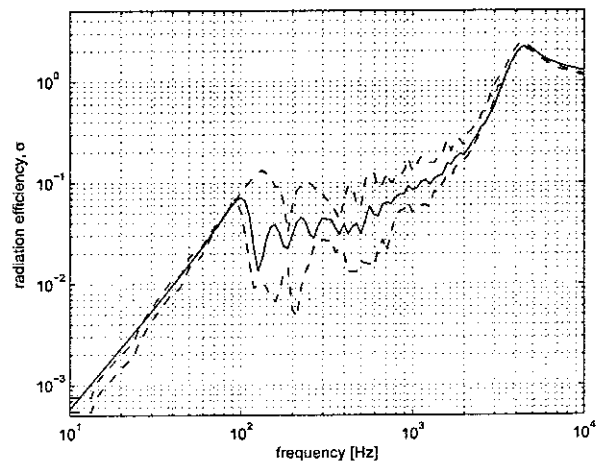

(c)

FIGURE 4.7: Range of radiation efficiency variation using 10/90 percentiles (– –) and average radiation efficiency (—) (aluminium plate, $\eta = 0.1$; (a). $0.65 \times 0.5 \times 0.03$ m, (b). $0.4 \times 0.75 \times 0.03$ m, (c). $0.8 \times 0.3 \times 0.03$ m).

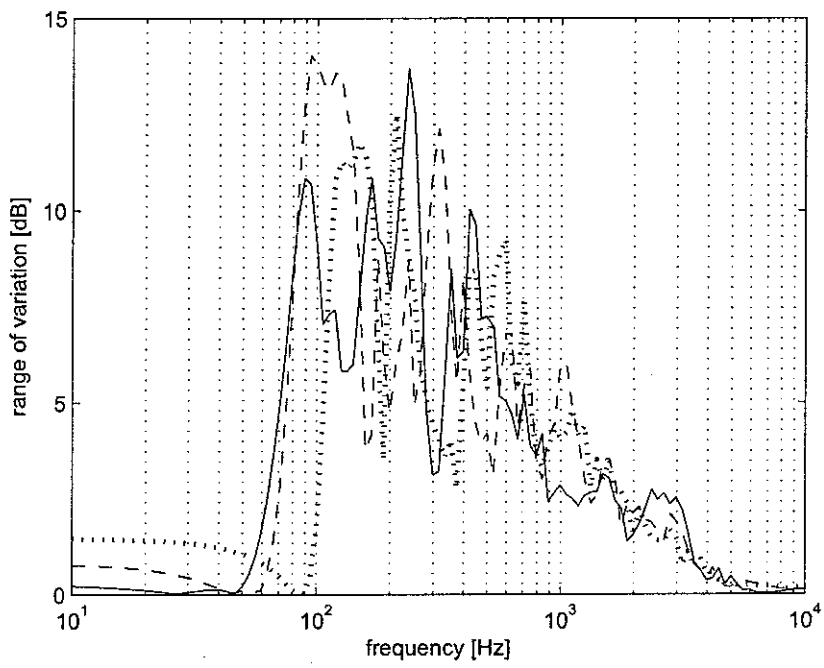

FIGURE 4.8: Variability of radiation efficiency from 10/90 percentiles with $\eta = 0.1$: $0.65 \times 0.5 \times 0.03$ m (—); $0.4 \times 0.75 \times 0.03$ m (– –); $0.8 \times 0.3 \times 0.03$ m ($\cdots$).

Chapter 5

Conclusions

Several methods for calculating the average radiation efficiency of baffled and unbaffled plates have been investigated. The radiation efficiency is calculated by applying a point force averaged over all positions on the plate. Cross-modal terms are not taken into account in the average radiation efficiency.

The spatial domain approach, due to the complexity and oscillatory nature of the integrand, needs a high resolution of integration segments to obtain an accurate result of the radiation efficiency of a simply supported baffled plate. The wavenumber domain approach has been found to be much more efficient. Using this method, the calculation time can be reduced significantly. The result shows that at very low frequencies, the slope of the average radiation efficiency of a baffled plate is 20 dB/decade. It is also found that for baffled plates, the FFT method [5] does not provide an efficient way for calculating the average radiation efficiency. Although the FFT itself is fast, the calculation time increases to calculate the modified Green's function required to avoid the singularity.

For the unbaffled plate case, the iterative method using the FFT [9] is used to develop the sound pressure field of a vibrating unbaffled, simply supported plate. It appears that this method has a convergence problem at low frequencies. It is also found that it can not cope with higher order plate modes. A method proposed by Laulagnet [8] gives a better result. It is found that the slope of the average radiation efficiency at very low frequencies is 40 dB/decade. Up to a frequency just below the critical frequency, the radiation efficiency of an unbaffled plate is lower than that of a baffled plate, the difference increasing as frequency is reduced. It also reveals that in the short circuiting

region, the baffled and unbaffled plates has frequency dependences of aprroximately 10 dB/decade and 20 dB/decade respectively.

The FFT method is not efficient in terms of calculation on a mode-by-mode basis. However, this method can be implemented to calculate the radiation efficiency from baffled plate for a single point force position. Selecting 20 points scattered over the surface of the plate, the variation of radiation efficiencies due to a single point force position appears to vary mainly in the corner and edge modes regions. It is also found that damping and plate dimensions have no significant effect on the variation.

References

[1] **Rayleigh, L.**, The Theory of Sound, 2nd edn., 1896.

[2] **Maidanik, G.**, *Response of ribbed panels to reverberant acoustic fields*, Journal of the Acoustical Society of America, Vol. 34, pp. 809–826, 1962.

[3] **Wallace, C. E.**, *Radiation resistance of a rectangular panel*, Journal of the Acoustical Society of America, Vol. 51, pp. 946–952, 1972.

[4] **Xie, G., Thompson, D. J.** and **Jones, C. J. C.**, *The radiation efficiency of baffled plates and strips*, Journal of Sound and Vibration, Vol. 280, pp. 181–209, 2005.

[5] **Williams, E. G.** and **Maynard, J. D.**, *Numerical evaluation of the Rayleigh integral for planar radiators using the FFT*, Journal of the Acoustical Society of America, Vol. 72, No. 6, pp. 2020–2030, 1982.

[6] **Williams, E. G.**, *A series expansion of the acoustic power radiated from planar sources*, Journal of the Acoustical Society of America, Vol. 73, No. 5, pp. 1520–1524, 1983.

[7] **Atalla, N., Nicolas, J.** and **Gauthier, C.**, *Acoustic radiation of an unbaffled vibrating plate with general elastic boundary conditions*, Journal of the Acoustical Society of America, Vol. 99, No. 3, pp. 1484–1494, 1996.

[8] **Laulagnet, B.**, *Sound radiation by a simply supported unbaffled plate*, Journal of the Acoustical Society of America, Vol. 103, No. 5, pp. 2451–2462, 1998.

[9] **Williams, E. G.**, *Numerical evaluation of the radiation from unbaffled, finite plates using the FFT*, Journal of the Acoustical Society of America, Vol. 74, No. 1, pp. 343–347, 1983.

[10] **Oppenheimer, C. H.** and **Dubowsky, S.**, *A radiation efficiency for unbaffled plates with experimental validation*, Journal of Sound and Vibration, Vol. 199, No. 3, pp. 473–489, 1997.

[11] **Fahy, F. J.** and **Thompson, D. J.**, *The effect of perforation on the radiation efficiency of vibrating plates*, Proceedings of the Institute of Acoustics, Vol. 26, 2004.

[12] **Nelisse, H., Beslin, O.** and **Nicolas, J.**, *A generalized approach for the acoustic radiation from a baffled of unbaffled plate with arbitrary boundary conditions, immersed in a light or heavy fluid*, Journal of Sound and Vibration, Vol. 211, No. 2, pp. 207–225, 1998.

[13] **Nolte, B.** and **Gaul, L.**, *Sound energy flow in the acoustic near field of a vibrating plate*, Journal of Sound and Vibration, Vol. 17, No. 4, pp. 269–277, 1996.

[14] **Mattei, P. O.**, *Sound energy by baffled and constrained plates*, Journal of Sound and Vibration, Vol. 179, No. 1, pp. 63–77, 1995.

[15] **Snyder, S. D.** and **Tanaka, N.**, *Calculating total acoustic power output using modal radiation efficiencies*, Journal of the Acoustical Society of America, Vol. 97, No. 3, pp. 1702–1709, 1995.

[16] **Li, W. L.** and **Gibeling, H. J.**, *Determination of the mutual radiation resistances of a rectangular plate and their impact on the radiated sound power*, Journal of Sound and Vibration, Vol. 229, No. 5, pp. 1213–1233, 2000.

[17] **Cremer, L., Heckl, M.** and **Ungar, E. E.**, Structure-borne sound, Springer, Berlin, 3rd edn., 2005.

[18] **Fahy, F. J.**, Sound and Structural Vibration: Transmission and Response, Academic Press, London, 1985.

[19] **Weisstein, E. W.**, *Fast Fourier Transform*, From MathWorld--A Wolfram Web Resource. http://mathworld.wolfram.com/FastFourierTransform.html.